Chemical Engineering Journal 498 (2024) 155592

Contents lists available at ScienceDirect

Chemical Engineering Journal

journal homepage: www.elsevier.com/locate/cej

Pleiotropy of biomineralized bacterial outer membrane vesicles in modulating immune systems for liver cancer therapy

Ying Luo, Zhongsheng Xu, Qianying Du, Lian Xu, Yi Wang, Jie Xu, Junrui Wang, Sijin Chen, Wenli Zhang, Bo Liu, Jia Liu, Dajing Guo *, Yun Liu *

Department of Radiology, Second Affiliated Hospital of Chongqing Medical University, Chongqing 400010, PR China

ARTICLE INFO

Keywords:
Outer membrane vesicle (OMV)
Metal ions
Ferroptosis
cCAS-STING
Immunotherapy
Liver cancer

ABSTRACT

The immune landscape of late-stage liver cancer is featured by severe immunosuppression that is characterized by poor immunogenicity, T-cell exhaustion, and infiltration of a large number of immunosuppressive cells, leading to compromised therapeutic efficacy of mainstream immunotherapies. Herein, we developed a pleiotropic immune cell mobilization strategy to modulate immune systems for immunosuppressive liver cancer therapy. In this study, immunogenic bacteria-derived outer membrane vesicles (OMVs) were exploited as a vector to deposit Cu and Mn with mixed valence states via one-step biomineralization, followed by platelet membrane camouflage, which are denoted as OPCM. Mechanistically, the pleiotropic OPCM possesses POD, CAT, and GPX-like activities, thereby achieving cGAS-STING activation, immunogenic ferroptosis, and tumor hypoxia alleviation, ultimately leading to initiation of the cancer immunity cycle, modulation of both innate and adaptive immune system, and reversion of immunosuppression. Notably, the combination with typical αPD-L1 treatment augmented the tumor suppression effect by amplifying the intensity of ferroptosis due to IFN-γ secretion by activated T cells. Overall, the metal biomineralized OPCMs in combination with αPD-L1 formed a closed-loop therapy that cycles from immunotherapy and ferroptosis therapy, providing new insights for treating immunosuppressive liver cancer.

1. Introduction

The efficacy of major immunotherapies is greatly hindered in solid tumors due to low patient response rate (10%~15%), especially in breast cancer and liver cancer [1–4]. Effective antitumor immunotherapy relies on multiple facets, including initiation of cancer immunity cycle (CIC), activation of the innate and adaptive immune system, and reversion of the tumor immunosuppressive microenvironment [5]. However, simultaneous activating masses of antitumor immune cells and reshaping the immunosuppressive tumor microenvironment (TME) in a sequential manner is extremely difficult. Current immunotherapy, such as immune checkpoint blockade (ICB), targets the adaptive immune system and aims to salvage exhausted T cells, neglecting major components from the innate immune system (antigen presenting cell (APC), natural killer (NK) cell, and macrophages) and the immunosuppressive network (M2 tumor associated macrophages (M2 TAMs)) in the TME [6]. In the TME, antigen presenting cell (APC), such as dendritic cell (DC), is the gatekeeper of the CIC, which presents tumor antigens to naive T cells and induces T cell differentiating into cytotoxic T cells. However, most of the DCs are malfunctioned due to the exhibition of an immature and immunosuppressive phenotype [7]. Consequently, the antitumor immunity mediated by T cells is compromised due to insufficient innate immune activation. In addition, the tumoricidal effects of other key immune cells from the innate immune systems, including NK cells and M1 TAMs, are suppressed [8]. Even worse, M1 TAMs can be differentiated into protumoral M2 phenotype, disabling the immune-mediated antitumor activity. To enhance the antitumoral efficacy of typical immunotherapy, the aforementioned innate immune cells and immunosuppressive cells should be targeted as well. Herein, a pleiotropic antitumor immunotherapeutic paradigm is desirable.

Fortunately, the cyclic GMP-AMP synthase-stimulator of interferon genes (cGAS-STING) signaling pathway is a key innate immune tuning pathway and acts as a bridge to link the innate and adaptive immune system by triggering the production of type 1 interferons (IFNs) and other inflammatory cytokines, leading to DC maturation, TAMs repolarization, and even natural killer (NK) cell activation in the tumor

* Corresponding authors.
E-mail addresses: guodaj@hospital.cqmu.edu.cn (D. Guo), yunliu@cqmu.edu.cn (Y. Liu).

https://doi.org/10.1016/j.cej.2024.155592
Received 6 June 2024; Received in revised form 8 August 2024; Accepted 6 September 2024
Available online 12 September 2024

microenvironment (TME) [9–13]. The consequential DC maturation results in T-cell activation and cytotoxic T cell (CTL) infiltration. On the other hand, the TAM repolarization reverses the immunosuppressive TME, augmenting antitumor immunity. Among all STING agonists, Mn^{2+}-involved agents has especially favored since it can independently activate cGAS, and induces the phosphorylation of both TBK1 and p65 independent of double-stranded DNA (dsDNA), leading to cGAS-STING activation and pleiotropic immune mobilization [14–18]. To boost Mn^{2+}-induced STING agonism, an adjuvant that can expose cytosol dsDNA is required. Catalytic agents, especially metal-based materials, have been applied to catalytic therapy by inducing reactive oxygen species (ROS) production, thus attacking mitochondria and nuclei, thereby exposing dsDNA in the cytosol [19–22]. Hence, we hypothesized that the introduction of Cu^{+} that possesses strong peroxidase (POD)-like activities may boost Mn^{2+}-induced cGAS-STING activation and amplify antitumor immunity. Moreover, metal ions with mixed valence states are supposed to exert stronger antitumor efficiency by exerting multiple enzyme-like activities. Regarding both Cu and Mn, Mn^{2+} and Cu^{+} in a low valence state possess peroxidase (POD)-like activities while Mn^{3+}, Mn^{4+}, and Cu^{2+} in a high valence state possess catalase (CAT)/glutathione peroxidase (GPX)-like activities. Thus, we hypothesized that Mn and Cu with mixed valence states possess ternary enzyme-like activities (POD, GPX, CAT), resulting in ROS production, GPX4 degradation, and O_2 generation, ultimately resulting in ferroptosis and hypoxia alleviation. Ferroptotic tumor cells can release abundant intracellular cytokines, damaged associated antigen molecules (DAMPs), and tumor associated antigens (TAAs) to promote DC maturation in synergy with type 1 IFNs, while hypoxia alleviation can reduce intratumoral hypoxia-inducible factor 1α (HIF-1α) expression, leading to TAM repolarization into M1 phenotype. It is worth noting that IFN-γ secreted by CTL and NK cells as a result of the activated STING pathway can inhibit the xc-system of tumor cells and further suppress the bioactivity of GPX4, thereby enhancing lipid peroxidation (LPO) accumulation and exacerbating ferroptosis of tumor cells [23,24]. Herein, a pleiotropic therapeutic paradigm was formulated between ferroptosis and cGAS-STING activation, leading to initiation of the CIC, modulation of both innate and adaptive immune system, and reversion of immunosuppression. However, the introduction of abundant free metal ions into human bodies poses a serious health threat, which will lead to metal toxicity and organ dysfunction. Precise transportation of metal ions into the targeted tumor sites and preventing premature leakage of metal ions are crucial for developing a bio-safe and feasible technique for immunomodulatory therapy.

Bacteria-derived outer membrane vesicle (OMV), secreted by Gram-negative bacteria, a neotype immune adjuvant or immune vaccine, holds great promise for boosting tumor immunotherapy [25,26]. OMV can initiate strong innate immune responses because OMV contains numerous pathogen-associated molecular patterns (PAMPs), such as peptidoglycan, lipopolysaccharide (LPS) and flagellin, and a growing body of evidence confirmed that OMV administration effectively mobilized multiple immune cells to resist tumor growth via various approaches, like promoting DC maturation and TAM re-polarization, inducing immunogenic pyroptosis, and even evoking trained antitumor immunity [27–31]. Inspired by the fact that OMV is negatively charged and embedded with vast biomolecules and proteins just as cytomembrane, we hypothesized that OMV may serve as a favorable nanocarrier to deposit multiple positively charged metal ions.

Herein, in this study, we first harvested OMVs from Escherichia coli (*E. coli*), followed by Cu and Mn deposition, which was denoted as OCM (OMV@Cu+Mn). Afterward, to shield the pristine OMVs from the body's immune defense and achieved active tumor target, the OCM was further decorated with platelet membrane (PM) by physical extrusion and renamed as OPCM (OMV@PM@Cu+Mn). On the one hand, PM displayed fewer antigens and lower immunogenicity compared with other cellular membranes, thereby avoiding immune recognition in the liver which is responsible for first pass elimination. On the other hand, the overexpressed P-Selectin and CD44 on the PM can specifically bind to CD44 receptors up-regulated on the surface of cancer cells as previous reported, thus enabling the active tumor target. The schematic figure of the synthetic process and the mechanistic illustration can be seen in Scheme 1. Mechanistically, upon the stealth effect of PM, OPCM selectively accumulated at the tumor site, followed by phagocytosis by tumor cells. Once getting into the tumor cells, Cu and Mn ions were subsequently released from the OMVs into the cytoplasm. On the one hand, glutathione (GSH) depletion, ROS production, and O_2 generation can be achieved due to the mixed valence state of Cu and Mn, leading to down-regulation of HIF-1α, inactivation of GPX4, accumulation of lipid peroxidation, and cytosol DNA exposure, leading to the alleviation of tumor hypoxia, initiation of tumor ferroptosis, and activation of the cGAS-STING signaling pathway. On the other hand, Mn^{2+} boosted the activation of the cGAS-STING signaling pathway by sensitizing the activities of various molecules in this molecular pathway. As a result, abundant immunogenic factors (CRT, ATP, HMGB1), TAAs, and type 1 IFNs can be produced and released due to broken cell membranes induced by LPO accumulation, and further awaken both the innate and adaptive immune systems by activating NK cells, re-polarizing M2 TAMs, promoting DC maturation, and recruiting cytotoxic T cells (CTLs) into the TME. Abundant IFN-γ secretion as a result of the massive immune stimulation further exacerbates tumor ferroptosis by down-regulating the GPX4 pathway, forming a closed-loop therapy. Specifically, Mn^{2+} possesses magnetic resonance imaging (MRI) performance and can realize theranostic purposes in a TME-responsive manner. This paradigm was proved to significantly amplify the therapeutic effect of anti-PD-L1 antibody (αPD-L1) to treat hepatocellular carcinoma (HCC) in two mouse models. As a proof of concept, this is the first study that applied OMVs as metal ion transporters by one-step biomineralization and identified the critical role of both Cu and Mn in inducing ferroptosis and ferroptosis-enhanced cGAS-STING activation for tumor pleiotropic immunomodulatory therapy.

2. Results and discussion

2.1. Characterization of various OMV-based nanodrugs

Firstly, pristine OMV from *E. coli* BL21 was extracted as previously reported, followed by one-step biomineralization of Cu and Mn ions, and coating of PM [29]. Next, a range of input concentrations of $CuCl_2$ and $MnCl_2$, ranging from 50 mM to 800 mM, were applied to assess the optimal loading capacity (LC) of OMVs for both Cu and Mn ions. The results of inductively coupled plasma-mass spectrometry (ICP-MS) indicated a dose-dependent increase of LC for both Cu and Mn. When the input concentration of Cu and Mn reached 800 mM, the LC reached ~6% for both metals (**Fig. S1**). The molar ratio of Cu and Mn in the OPCM sample was determined to be approximately 1.2:1 by ICP-MS. Based on this result, 800 mM input of Cu and Mn was chosen to synthesize OPCM for the following experiments. As shown in Fig. 1a, the morphology of pristine OMVs was spherical under transmission electron microscopy (TEM). After the coating of PM, a double membrane structure was identified under TEM. Beyond that, sodium dodecyl sulfonate-polyacrylamide gel electrophoresis (SDS-PAGE) assay confirmed that protein bands from the original PM and OMV were reserved in the OPCM, indicating the co-existence of both PM and OMV (Fig. 1c). In addition, TEM mapping was done to verify the elemental composition of the ultimate OPCM. As indicated in Fig. 1d, the C, O, Cu, and Mn elements were shown around the OPCM. Dynamic light scattering (DLS) revealed that the hydrodynamic size of OMVs, OP, OCM, and OPCM was 228, 396.9, 412.3, and 506.6 nm, respectively (Fig. S2). The results of DLS demonstrated that the coating of PM and deposition of Cu and Mn ions enlarged the diameter of OMVs, which might be ascribed to the aggregation of OPCM induced by metal ion deposition. The zeta potentials of OMV, PM, OP, OCM, and OPCM were all negative, among which OP displayed the most negative value, and OCM displayed the

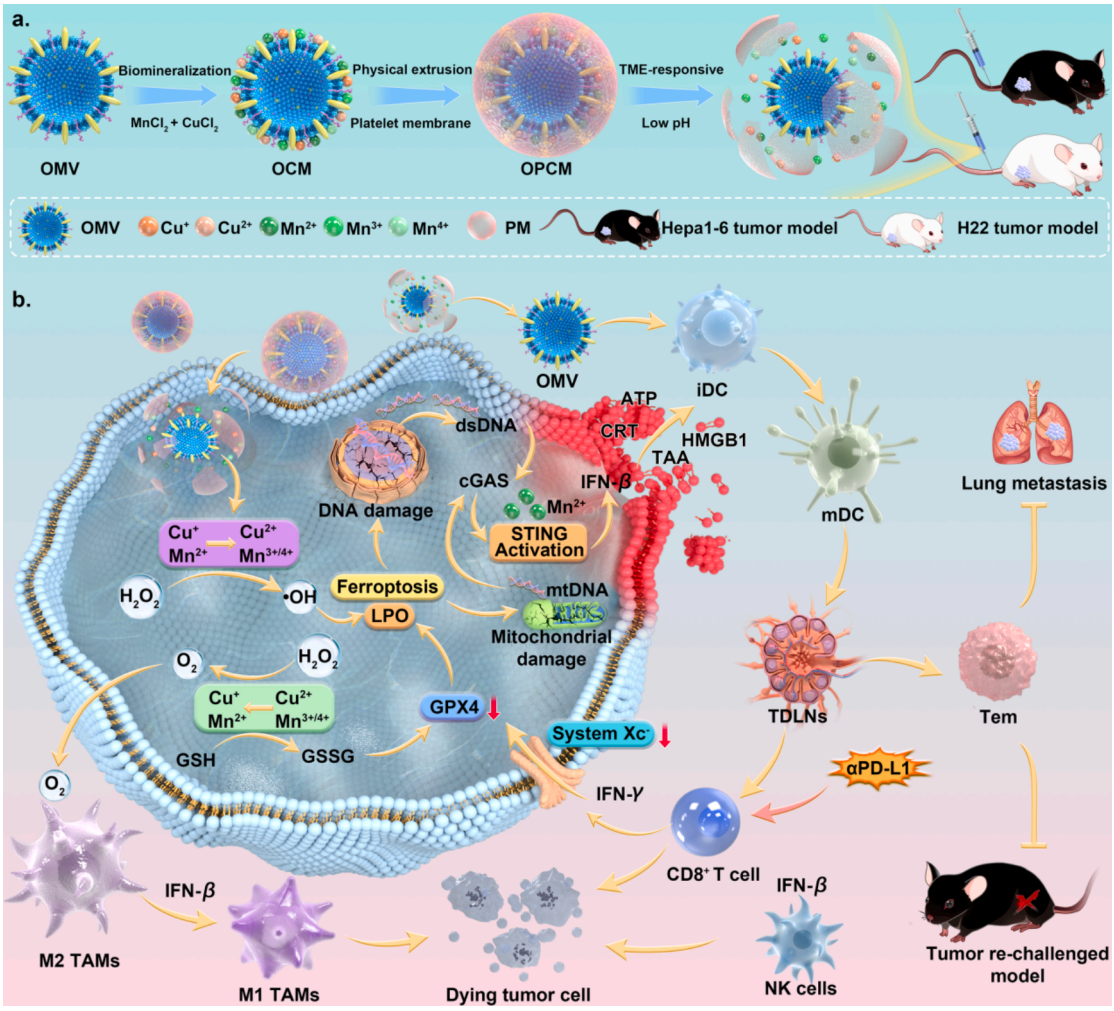

Scheme.1. Schematic illustration of the synthesis of OPCM and OPCM-induced pleiotropic immune mobilization strategy in synergy with αPD-L1.

least negative value, indicating the successful loading of Cu and Mn ions in the OPCM (Fig. 1b). The elemental composition of the OPCM was detected further by X-ray photoelectron spectroscopy (XPS), which revealed the co-existence of Cu and Mn elements in the OPCM (Fig. 1e). Interestingly, after analysis of Cu2P and Mn2P, we identified two strong binding energy peaks (932.18 and 934.28 eV) corresponding to Cu^{+} and Cu^{2+}, and three strong binding energy peaks (640.88, 646.18, and 642.28 eV) that were assigned to Mn^{2+}, Mn^{3+}, and Mn^{4+} (Fig. 1f, g). The presence of Cu and Mn ions with mixed valence states was believed to be correlated with a series of redox reactions that took place in the process of metal ion biomineralization due to the presence of polysaccharide, protein molecules, and biomacromolecules anchored on the surface of pristine OMV. The X-ray powder diffraction (XRD) pattern showed the amorphous structure of OPCM (Fig. S3). All the above results demonstrated that OPCM was successfully synthesized *via* one-step biomineralization.

In addition, the electrochemically active area (ECSA) of biomineralized OMVs was measured through the double-layer capacitance method (Fig. 1**h, i, j, and** Fig. **S4**). Compared with the mono-metallic biomineralized OMV, the dua-metallic biomineralized OMV obtained the highest value of ESCA (0.0481 mF/cm^2), indicating that the dual-metallic biomineralized OMV enabled the most abundant active sites, which was mainly attributed to the introduced Cu ions with high catalytic activity. Metal ions in a low valence state with POD-like activities decompose H_2O_2 into hydroxyl radical (•OH) under an acidic environment, while metal ions in a high valence state with CAT/GPX-like activities, promote O_2 production and GSH degradation into oxidized glutathione disulfide (GSSG), thereby alleviating intratumoral hypoxia and preventing ROS elimination.[32] Owning to the co-existence of Cu^{+}, Cu^{2+}, Mn^{2+}, Mn^{3+}, and Mn^{4+}, high content of H_2O_2 and GSH in tumor cells and TME were supposed to be catalyzed into O_2, ·OH, and GSSG. Based on the results of the electrochemical test, the factual catalytic activity of OPCM was validated *via* 3,3,5,5-tetramethylbenzidine (TMB), 5,5′-dithiobis (2-nitrobenzoic acid) (DTNB), and a dissolved oxygen monitor. TMB was applied to evaluate the POD-like activity of OPCM. The intermediate ·OH could oxidize TMB from colorless to blue with obvious characteristic light absorption at about 575 nm (Fig. S5a). Absorption at this wavelength was enhanced in a concentration-dependent manner with the addition of H_2O_2, which indicated that OPCM had a favorable chemo-dynamic effect *via* the Fenton-like reaction. A dissolved oxygen monitor was employed to confirm the CAT-like activity of OPCM. Fig. S5b showed a time-dependent change of O_2 generation in three groups with different concentrations of OPCM + H_2O_2, among which 400 μg/mL OPCM displayed the maximum O_2 increase, suggesting the ability of OPCM to catalyze O_2 generation for alleviating intratumoral hypoxia status. To evaluate the GPX-like activity of OPCM, DTNB was chosen as an indicator, since DTNB can measure GSH content due to the weakening of its characteristic UV–Vis absorption peak at 412 nm when reacting with GSH. As revealed by Fig. S5c, a time-dependent decrease pattern of GSH content was identified, which indicated that the as-synthesized OPCM possessed GPX-like activity and may potentiate ROS production and GPX4-dependent ferroptosis in tumor cells. Taken together, the obtained OPCM could not only decompose H_2O_2 but also could deplete GSH, leading to simultaneous O_2

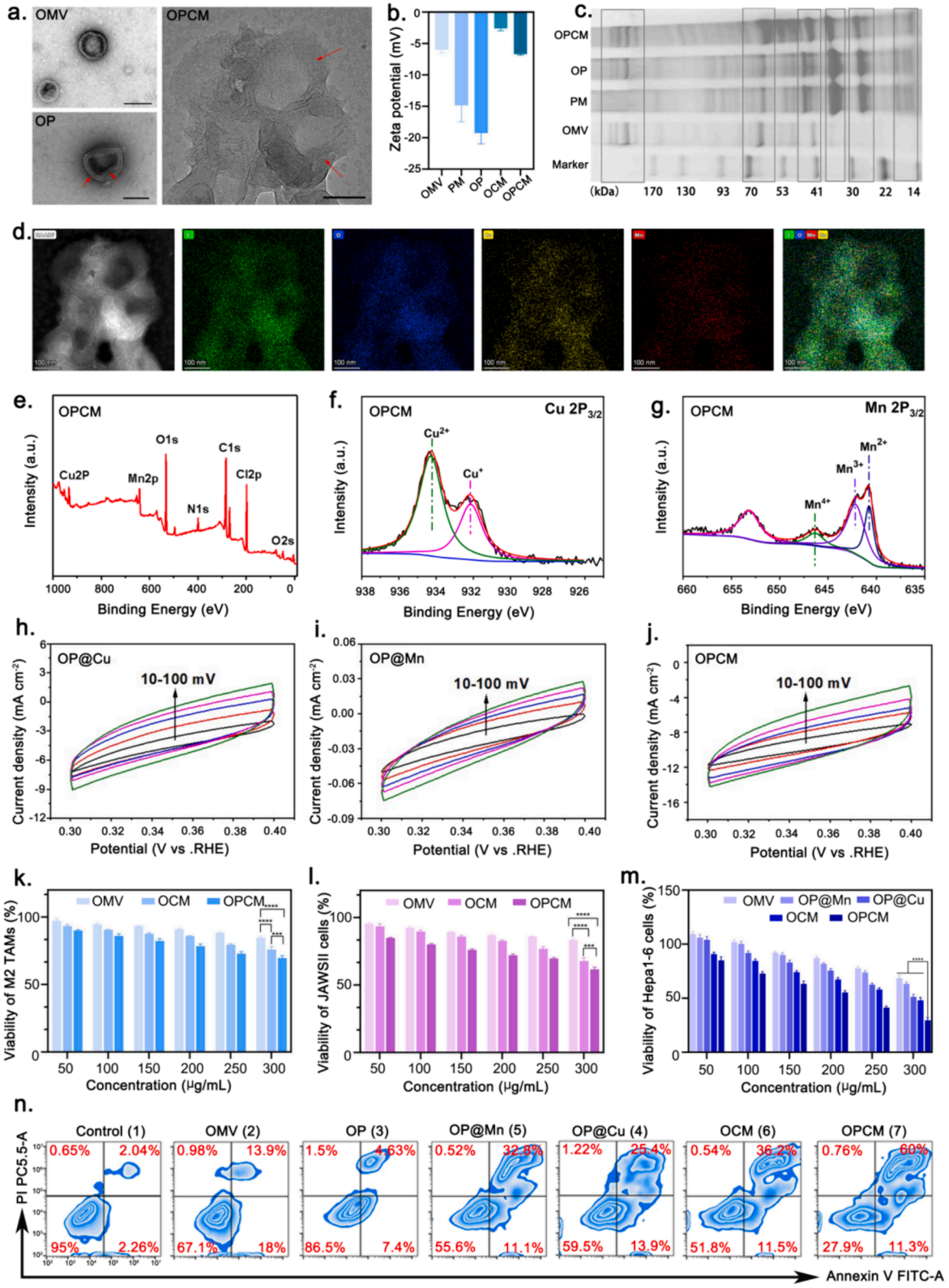

Fig. 1. Characterization of various OMV-based nanodrugs. (a) TEM of OMV, OP, and OPCM. Scale bar: 100 nm. (b) Zeta potential of OMV, PM, OP, OCM, and OPCM. Data are shown as the mean values ± SD (n = 5). (c) SDS-PAGE assay of OMV, PM, OP, and OPCM. (d) Elemental mapping of OPCM. Scale bar: 100 nm. (e, f, g) XPS survey spectra and XPS spectra of Cu2P and Mn2P. (h, i, j) CV curves of OP@Cu, OP@Mn, and OPCM of various electrodes in the non-Faradaic capacitive range at the scan rate of 10 ~ 100 mV s^{-1}. (k, l) Cell viability of M2 TAMs, JAWSII cells after co-incubation with OMV, OCM, or OPCM. Data are shown as the mean values ± SD (n = 5). (m) Cell viability of Hepa1-6 cells after co-incubation with OMV, OP@Mn, OP@Cu, OCM, or OPCM. Data are shown as the mean values ± SD (n = 5). (n) FCM analysis of Hepa1-6 cells apoptosis after various treatments. All the statistical significance was analyzed by ANOVA. * $p < 0.05$, ** $p < 0.01$, *** $p < 0.001$, **** $p < 0.0001$, ns, not significant.

generation, and ROS production, implying great promise for anti-tumor application. Subsequently, the TME-responsive release behavior of OPCM was measured by ICP-MS. Fig. S6 showed distinct acid-responsive release behavior of Cu and Mn, which may be attributed to the acid-responsive degradation of PM and OMV. The results proved that Cu and Mn ions could be released in tumor cells accurately and efficiently.

Encouraged by the ternary enzyme-like activities, the biosafety and tumor-killing effect of OMV-based nanodrugs were further evaluated at the cellular level. M2 TAMs and JAWSII cells were chosen to test the biocompatibility of OMV-based nanodrugs on non-tumor cells. As revealed in Fig. 1**k** and **1l**, CCK-8 results showed that the pristine OMV, OCM, and OPCM had no obvious cytotoxicity on M2 TAMs and JAWSII cells even when the concentration reached 300 μg/mL. The cytotoxicity of OCM on RAW264.7 and JAWSII cells was determined to be lower than that of OPCM, and higher than that of OMV, which might be ascribed to PM-mediated intracellular uptake of metal-deposited OPCM. To test the antitumor effect of OPCM on Hepa1-6 cells, different concentrations of OMV, OP@Mn, OP@Cu, OCM, and OPCM were incubated with Hepa1-6 cells for 24h. Fig. 1m revealed that the pristine OMV at 300 μg/mL lowered the viability of Hepa1-6 cells to about 70%, OP@Mn and OP@Cu at the same concentration lowered the viability to about 60% and 50% respectively, OCM lowered the viability to about 50%, OPCM considerably lowered the viability to around 30%, suggesting the effective tumor-killing effect of bimetallic biomineralized OPCM. More specifically, OMVs mineralized with two metal ions were obviously better than those mineralized with a single metal ion. To summarize, compared with the cytotoxicity on RAW264.7 and JAWSII cells, OMV, OCM, and OPCM exerted stronger cytotoxicity on Hepa1-6 cells, which might be attributed to excessive GSH and H_2O_2 in tumor cells. Furthermore, the existence of PM on the outer shell of OPCM facilitated intracellular uptake of OPCM due to the ligand-receptor interaction, leading to more metal ion intake compared with non-tumor cells. Based on the results of CCK-8, 300 μg/mL of OMV, OP, OCM, and OPCM were used to evaluate other cellular performance.

Effective intracellular uptake of OPCM in tumor cells is a prerequisite for achieving desirable antitumor efficacy. Therefore, the intracellular uptake of DiI-labeled OPCM was assessed by confocal laser scanning microscopy (CLSM). Fig. **S7a** displayed a time-dependent increase of red fluorescence (FL) signals around the DAPI-stained nuclei, suggesting that the DiI-labeled OPCM was effectively engulfed by Hepa1-6 cells. This phenomenon was also verified by flow cytometry (FCM) as demonstrated in Fig. S7b and S7c, suggesting that tumor cells could effectively engulf OPCM.

To further evaluate the inhibitory effect of various OMV-based nanomaterials on tumor cell growth, Calcein-AM (green)/propidium iodide (PI) (red) kit and Annexin V-FITC/PI assay were conducted and observed by both FL microscopy and FCM. According to the results of live/dead cell staining under FL microscopy, the control, OMV, and OP groups did not exhibit obvious cell damage, indicating that OMV and OP without metal ions were biocompatible (Fig. S8). The OP@Cu and OP@Mn treatment moderately increased the number of PI-positive dead cells, while the OCM group displayed a significantly increased number of dead cells, suggesting that the biomineralization of both Cu and Mn on the OMVs increased cytotoxicity on cancer cells. Compared with the above four groups, the last OPCM group exhibited the least Calcein-AM-stained live cells and the most prevalent PI-stained dead cells, indicating that OPCM possessed the strongest anticancer efficacy. The results of FCM were in line with the result of live/dead cell staining. (Fig. 1n).

Taken together, the as-synthesized OPCM was successfully synthesized, which possessed a typical membrane structure with vast bacterial biomacromolecules and platelet proteins, ternary enzyme-like activities (POD-like, CAT-like, and GPX-like activities), pH responsiveness, and considerable anti-tumor effect, which might be due to the metal ion-induced tumoricidal activity and the PM-mediated intracellular uptake.

2.2. OPCM-initiated immunogenic ferroptosis and cGAS-STING activation

Given the favorable ternary enzyme-like activities, distinct cellular uptake behavior, and effective tumoricidal effect of OPCM validated in the above studies, the antitumor therapeutic mechanism of OPCM was further evaluated at the cellular level. First, ·OH generation was detected using the 2,7-dichlorodihydrofluorescein diacetate (DCFH-DA) probe since non-fluorescent DCFH-DA can be converted into fluorescent DCF by ROS oxidization. Specifically, a small-molecule lipophilic antioxidant, Fer, was added to the OPCM group to antagonize ferroptosis induction. The result of CLSM revealed that OMV group displayed negligible DCFH-FITC FL signals, while the OCM and OPCM groups exhibited greater DCFH-FITC FL signals, with the OPCM showing the strongest FL signals which were reduced by the addition of Fer, suggesting that the biomineralization of both Cu and Mn potentiated ROS production in Hepa1-6 cells and the initiation of ferroptosis (Fig. 2**a**). Accordingly, a similar result was observed via FCM (Fig. S9). It is reported that the overproduction of ROS results in lipid peroxidation (LPO) and mitochondrial membrane damage, leading to ferroptosis. Therefore, OPCM-induced LPO was assessed by a BODIPY-C11 fluorescent probe (581/591 nm) which is a lipid-soluble fluorescent indicator of LPO. During the LPO, the BODIPY-C11 dye changes from the aggregate state with red FL to the monomer state emitting green FL. The pristine OMVs had little effect on the LPO of Hepa1-6 cells, while cells cultured with the OCM and OPCM emitted more intense green FL signals, suggesting that the biomineralization of Cu and Mn ions on the OMVs induced LPO and played a crucial role in initiating tumor ferroptosis (Fig. 2b). Similar to the result of ROS detection, the intensity of LPO was reduced by the addition of Fer. These results collectively demonstrated that OPCM successfully induced cancer cell ferroptosis as shown by ROS production and LPO.

Experiments *in vitro* showed that the OPCM was capable of consuming GSH which is an endogenous antioxidant [33]. Depletion of GSH in tumor cells inactivates GPX4, resulting in an imbalance of redox reactions and then the accumulation of LPO, and subsequent ferroptosis [34]. Therefore, we further determined whether the OPCM activated the GPX4-related ferroptotic pathway. As shown in Fig. **S10**, the OCM and OPCM groups exhibited distinct reduced levels of intracellular GSH content compared to the control and OMV groups, demonstrating the GPX-like activity of OPCM. To test whether GSH consumption induced by OPCM leads to GPX4 degradation, a western blot (WB) was conducted. The result showed that the expression of GPX4 protein was declined in the OCM and OPCM groups compared to the control and OMV group, suggesting that OPCM contributed to ferroptosis *via* GPX4 degradation in addition to ROS production (Fig. 2c and Fig. S11).

It was reported that overexpression of intracellular ROS broke the integrity of the mitochondrial membrane, leading to the decrease of mitochondrial membrane potential (MMP) and the release of mitochondrial DNA (mtDNA) [35]. To further assess OPCM-induced mitochondrial damage, the mitochondrial function was evaluated by JC-1 dye that can monitor MMP change. When the positive charge of cell membrane potential declines, the JC-1 dye changes from the aggregate state (red color fluorescence) to the scattered state (green color fluorescence). According to the results of CLSM, compared with the control and OMV group, cells cultured with OCM and OPCM displayed a distinct increase in green FL signals and a decrease in red FL signals, suggesting that the JC-1 dye changed from the aggregate state to the scattered state (Fig. **S12**). The result of FCM was in accordance with the CLSM results as shown in Fig. S13, illustrating that OPCM treatment broke the mitochondrial membrane integrity and declined the MMP of Hepa1-6 cells, which might result in the release of mtDNA into the cytosol. The production of ROS was believed to attack nuclear DNA in several studies and led to DNA damage and dsDNA exposure in cytosol [20,36]. To confirm DNA damage, γ-H2AX was used as a DNA damage marker. According to the immunofluorescence (IF) results of γ-H2AX, OCM and

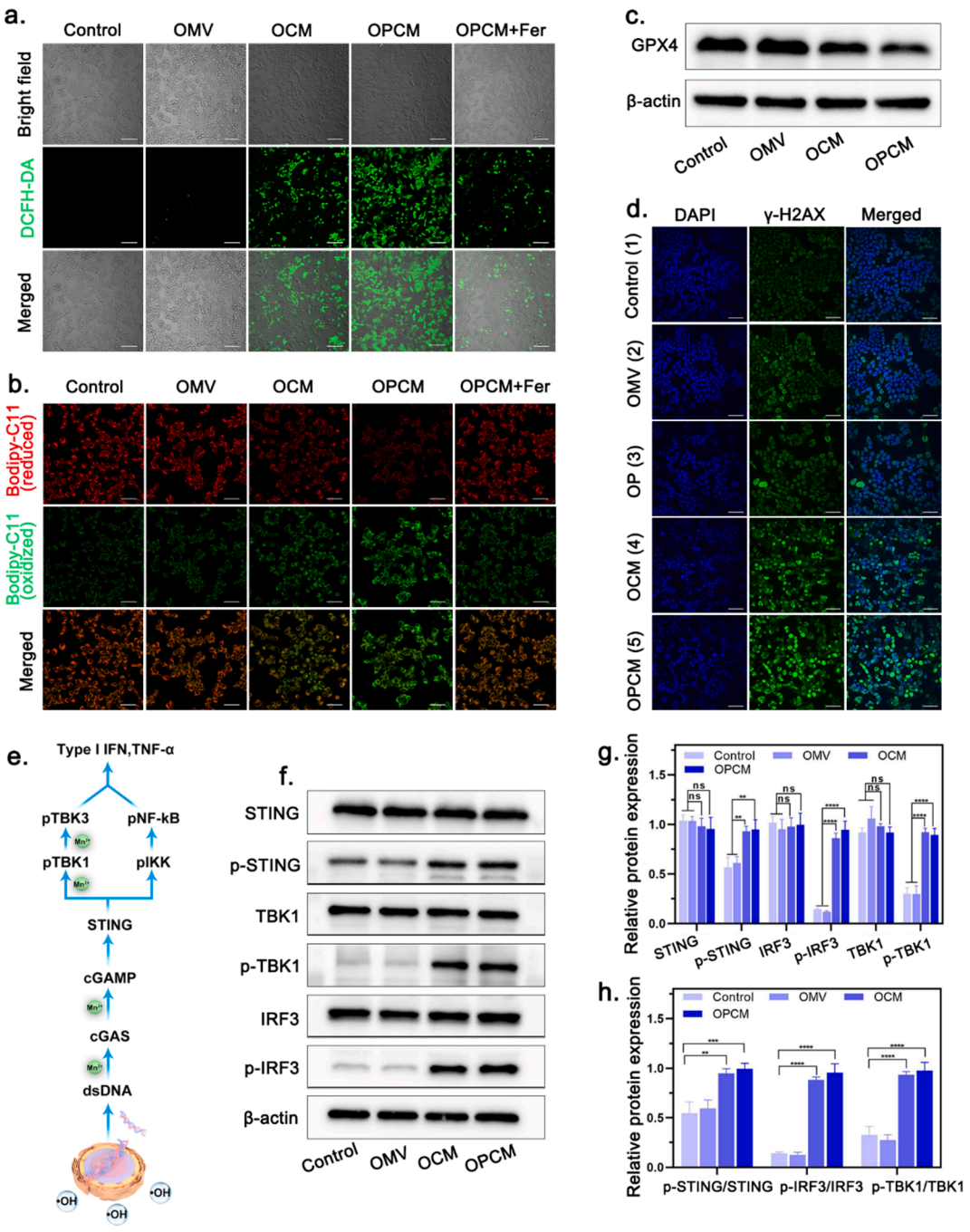

Fig. 2. The mechanism of ferroptosis induction and cGAS-STING activation *in vitro*. (a) CLSM of ROS analysis induced by PBS, OMV, OCM, OPCM, and OPCM+Fer respectively. Scale bar: 50 μm. (b) LPO stained with green fluorescent BODIPY-C11 in Hepa1-6 cells after incubation with PBS, OMV, OCM, OPCM, OPCM+Fer, scale bar: 50 μm. (c) WB analysis of GPX4 expression in Hepa1-6 cells after treatment with PBS, OMV, OCM, or OPCM, respectively. (d) CLSM images of γ-H2AX and CRT expression in Hepa1-6 cells after treatment with PBS, OMV, OP, OCM, or OPCM. Scale bar: 50 μm. (e) The schematic diagram of ferroptosis-induced cGAS-STING signaling pathway activation. (f, g) WB analysis of key protein expression in the cGAS-STING signaling pathway and the corresponding quantitative analysis. Data are shown as the mean values ± SD (n = 3). (h) The ratio of phosphorylated proteins versus non-phosphorylated proteins in the cGAS-STING signaling pathway in different treatment groups. Data are shown as the mean values ± SD (n = 3). All the statistical significance was analyzed by ANOVA. * $p < 0.05$, ** $p < 0.01$, *** $p < 0.001$, **** $p < 0.0001$, ns, not significant.

OPCM exhibited greatly enhanced green γ-H2AX FL signals compared to the control, OMV, and OP groups, hinting that the bimetallic biomineralized OCM and OPCM effectively induced DNA damage via ROS, which led to cytosol dsDNA exposure (Fig. 2d, Fig. S14).

Interestingly, cytosol dsDNA exposure is not only a result of intracellular ROS attack but also an activator of the cGAS-STING signaling pathway which plays a prominent role in the cancer immunity cycle by producing pro-inflammatory cytokines, such as type 1 IFN. Hypothetically, the cGAS-STING signaling pathway could also be synergistically activated by Mn^{2+} anchored on the OPCM as reported by previous studies. Hence, the expression levels of STING, p-STING, TBK1, p-TBK1, IRF3, and p-IRF3 were measured and corresponding statistical analyses were conducted. The schematic diagram of cGAS-STING activation is displayed in Fig. 2e. As demonstrated in Fig. 2f and 2g, the OMV treatment had little impact on the expression level of all the above six proteins just as the control group. The bimetallic biomineralized

OCM and OPCM showed insignificant influence on the expression of non-phosphorylated proteins (STING, TBK-1, IRF3), but augmented the expression of phosphorylated proteins (p-STING, p-TBK1, and p-IRF3). Through statistical analysis, the expression ratio of phosphorylated proteins versus non-phosphorylated proteins was significantly increased in the OCM and OPCM groups compared with the control and OMV groups, suggesting that the bimetallic biomineralized OCM and OPCM successfully activated the cGAS-STING signaling pathway (Fig. 2h).

To summarize, GSH depletion and ROS generation could be achieved due to the mixed valence states of Cu and Mn in OCM or OPCM, thus enabling tumor cells to undergo non-ferrous ferroptosis *via* inactivation of GPX4 and accumulation of LPO. In this process, the mitochondrial membrane was broken and the intranuclear DNA and mitochondrial DNA were damaged, leading to the cytosol mtDNA and dsDNA exposure, which might be conducive to activating the cGAS-STING signaling pathway. Notably, ferroptotic cancer cells are known to be immunogenic as the affected cells could release TAAs, and damage-associated molecular patterns (DAMPs), ultimately leading to antitumor immune activation. Therefore, the immunostimulatory effect of OPCM will be assessed and discussed in the following sections.

2.3. Exploration of ICD and immune cell regulation in vitro

Ferroptosis was reported to be immunogenic as numerous studies proved that abundant DAMPs (ATP, CRT, and HMGB1) are released from cell membrane rupture due to LPO accumulation, which promotes immune stimulation, such as DC maturation and TAM re-polarization [37]. In addition, the end-product of the cGAS-STING signaling pathway, type 1 IFN, was reported to mobilize multiple immune cells to exert tumoricidal effects. Furthermore, OMVs were also confirmed to be a strong immune adjuvant for immune stimulation. Therefore, the immune stimulatory effects of OPCM were examined on DCs and TAMs.

Fig. 3**a and 3b** elucidated the co-culture system of Hepa1-6 cells and DCs or TAMs respectively. The Hepa1-6 cells were placed on the upper chamber, while DCs or TAMs were seeded on the bottom of the six-well plate. As demonstrated in the FCM results, compared to the control group, the proportion of matured DCs was increased by 3.1-, 2.6-, 5.4-, and 6.6-fold in the OMV, OP, OCM, and OPCM groups, respectively, which showed that all the OMV-based nanodrugs were capable of inducing ICD and therefore promoting DC maturation and activating cellular antitumor immunity (Fig. 3c, 3d). Notably, the population of $CD80^+CD86^+$ cells in the OPCM group was the largest and 6.6-fold higher than that of the control group, suggesting that metal ions with mixed valence states played a dominant role in DC maturation.

The cytokine secretion level was also measured to confirm the ICD effect and DC maturation. Firstly, the ICD effect of OPCM on CRT expression was examined by IF staining. As revealed by Fig. **S15**, the OCM and OPCM groups displayed more green FL signals in comparison with the control group, OMV group, and OP group, suggesting the exposure of CRT induced by OCM and OPCM. Subsequently, we decided to further measure the secretion level of another two DAMPs, ATP and HMGB1, *via* enzyme-linked immunosorbent assay (ELISA). Type 1 IFN, and typical pro-inflammatory cytokines secreted by matured DCs, IL-6 and TNF-α were also tested *via* ELISA. The secretion levels of ATP and HMGB1 were distinctly higher in the OCM and OPCM groups than other groups, confirming the ICD effect of metal-deposited OMVs (Fig. 3e, 3f). The secretion level of type 1 IFN was consistent with the results of ATP and HMGB1 (Fig. 3g). There was a little variation of type 1 IFN among the control, OMV, and OP group. The OCM and OPCM groups remarkably enhanced the secretion level of type 1 IFN, suggesting the activation of the cGAS-STING signaling pathway. IL-6 and TNF-α were also higher in the OCM and OPCM groups than other groups, illustrating the effective DC maturation induced by bimetallic biomineralized OMVs (Fig. 3h, 3i). Notably, the secretion levels of IL-6 and TNF-α were slightly higher in the OMV and OP groups than those in the control group, which might be ascribed to the intrinsic immunostimulatory effect of OMV on immature DCs.

Next, the immunostimulatory effect of OMV-based nanodrugs on M2 TAMs was assessed. The OMV, OP, OCM, and OPCM groups all displayed higher $CD80^+$ cells than the control group, among which the OPCM displayed the highest proportion of $CD80^+$ cells among which the OPCM displayed the highest proportion of $CD80^+$ cells (74.2%) which indicated the enhancement of M1 TAMs **(**Fig. 3**j, 3k)**. Conversely, the number of $CD206^+$ cells was significantly lowered in all four intervention groups, among which the OPCM group displayed the minimum number of $CD206^+$ cells, suggesting that all the OMV-based nanodrugs were capable of decreasing the number of M2 TAMs (Fig. 3l, 3m). The secretion levels of ATP, HMGB1, and type 1 IFN in the coculture system of Hepa1-6 and TAMs followed the same pattern just as that of Hepa1-6 and DCs. The bimetallic biomineralized OCM and OPCM significantly enhanced the secretion of ATP, HMGB1, and type 1 IFN (Fig. 3n, 3o, 3p). In addition, we measured classical anti-inflammatory cytokine, IL-10, secreted by M2 TAMs, and classical pro-inflammatory cytokine, IL-12, secreted by M1 TAMs, to further verify the TAM re-polarization effect induced by OCM and OPCM. As expected, the secretion of IL-10 was significantly reduced in the OCM and OPCM groups, while the secretion of IL-12 was remarkably enhanced in these two groups, suggesting the successful re-polarization of M2 TAMs into M1 TAMs (Fig. 3q, 3r).

In short, the as-synthesized OMV, OP, OCM, and OPCM could all promote DC maturation and TAM re-polarization with the OPCM exerting the greatest immune activation effect. The potent immunostimulatory effect of OPCM might be ascribed to the collective effort induced by PAMPs anchored on OMVs and Cu and Mn-induced cGAS-STING activation and immunogenic ferroptosis. Inspired by the results of the *in vitro* experiments, we hypothesized that the OPCM might serve as a potent immune adjuvant to exert antitumor immunity in combination with typical immunotherapy in the following *in vivo* studies.

2.4. Exploration of anti-tumor effect in vivo

Based on the satisfactory inhibitory effect of OMV-based nanodrugs on tumor cells *in vitro*, the in-depth anti-tumor effect *in vivo* was further investigated in two mouse models, including C57BL/6J and BALB/c mice. To be specific, Hepa1-6 cells were inoculated into the right flank of C57BL/6J mice, while H22 cells were inoculated into the right flank of BALB/c mice.[38] The treatment protocol is depicted in Fig. 4**a**. As a crucial immunosuppressive factor in the TME, high expression of PD-L1 could trigger malfunction of CTL and compromise T cell-related tumoricidal effect. Encouraged by the efficient tumor-killing effect as demonstrated in the above *in vitro* studies, a commonly used immunotherapeutic agent, αPD-L1, was applied to synergize with OPCM to boost the pleiotropic immune stimulation effect of OPCM and concurrently induce tumoricidal effects on liver cancer models. The mice were divided into five groups, including the control, OMV, αPD-L1, OPCM, and the combination of αPD-L1 and OPCM. Firstly, we analyzed the antitumor effect of the four intervention groups on C57BL/6J mice. The body weight of mice in all groups showed no abnormalities, suggesting that all the treatments exhibited no obvious systemic toxicity (Fig. 4b). As revealed by the growth of tumor relative volume, the combination group (αPD-L1 + OPCM) presented a higher tumor inhibiting capacity compared with the other groups (Fig. 4c). The results of the individual tumor growth curve, the representative photos of mice during treatment, the photograph and average weight of extracted tumors in each group, and the corresponding tumor inhibition rates were consistent with the outcome of relative tumor volume as shown in Fig. 4d, 4e, S16, and S17. Afterward, terminal deoxynucleotidyl transferase dUTP nick end labeling (TUNEL), proliferating cell nuclear antigen (PCNA), and hematoxylin and eosin (H&E) staining assays were conducted to assess the extent of tumor apoptosis, tumor proliferation, and tumor necrosis. As demonstrated in Fig. 4j, prevalent red PCNA FL signals were shown in the control group. The PCNA FL signals were slightly diminished in the OMV and αPD-L1 groups, while the FL signals were largely reduced in

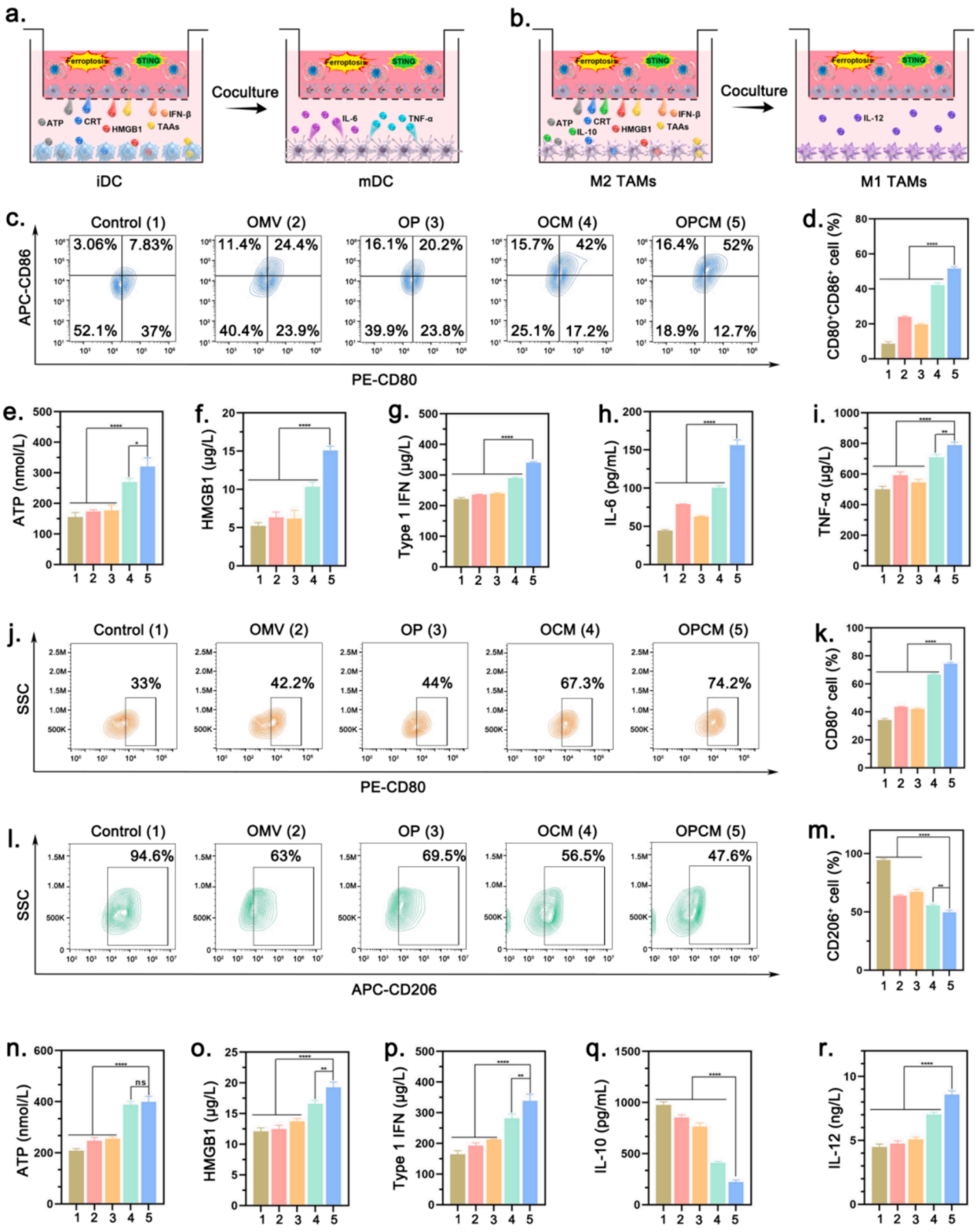

Fig. 3. The immune stimulation assay *in vitro*. (a, b) The schematic diagram of the co-culture system of Hepa1-6 cells with DCs, and TAMs, respectively. (c, d) Representative FCM results of DC maturation after different treatments and the corresponding quantitative analysis. Data are shown as the mean values ± SD (n = 3). (e, f, g, h, i) ELISA test of the secretion level of ATP, HMGB1, Type 1 IFN, IL-6, and TNF-α in the coculture system of Hepa1-6 cells and DCs. Data are shown as the mean values ± SD (n = 3). (j, k, l, m) Representative FCM results of the expression of CD80 and CD206 in TAMs after different treatments and the corresponding quantitative analysis. Data are shown as the mean values ± SD (n = 3). (n, o, p, q, r) ELISA test of the secretion level of ATP, HMGB1, Type 1 IFN, IL-10, and IL-12, respectively. Data are shown as the mean values ± SD (n = 3). All the statistical significance was analyzed by ANOVA. * $p < 0.05$, ** $p < 0.01$, *** $p < 0.001$, **** $p < 0.0001$, ns, not significant.

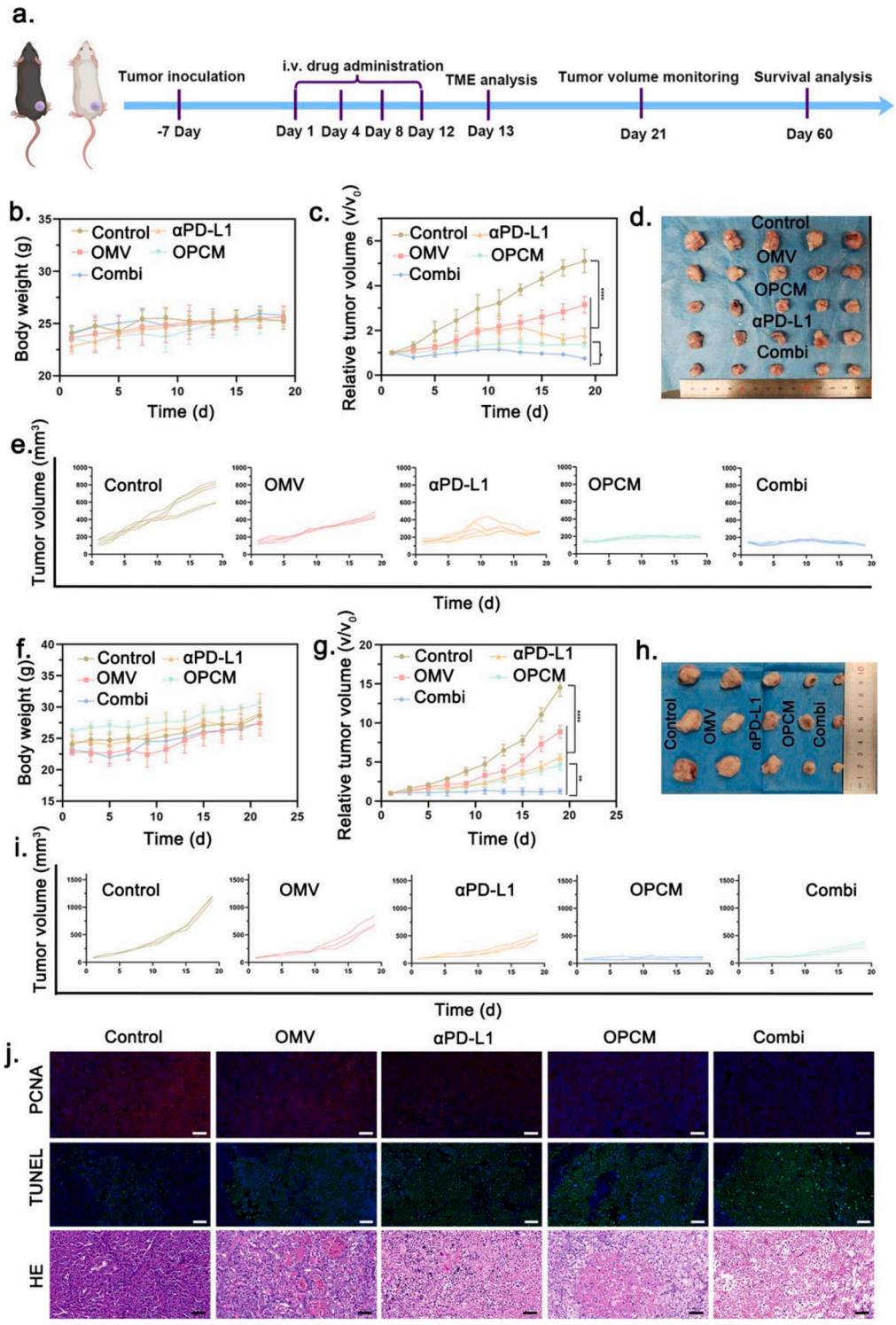

Fig. 4. Antitumor evaluation *in vivo*. (a) Schematic diagram of the experimental procedure for exploring antitumor effects of different treatments on Hepa1-6 cell inoculated C57BL/6J mice and H22 cell inoculated BALB/c mice. (b) Average body weight change of C57BL/6J mice during the observation duration. Data are shown as the mean values ± SD (n = 5). (c) The growth curve of relative tumor volume in different treatment groups of C57BL/6J mice. Data are shown as the mean values ± SD (n = 5). (d) The digital photograph of extracted tumors at sacrifice in C57BL/6J mice on the 21st day. Data are shown as the mean values ± SD (n = 5). (e) The individual tumor growth curve in each treatment group of C57BL/6J mice. Data are shown as the mean values ± SD (n = 5). (f) The average change of mice body weight in different treatment groups of BALB/c mice. Data are shown as the mean values ± SD (n = 3). (g) The relative tumor volume change in different treatment groups of BALB/c mice. Data are shown as the mean values ± SD (n = 3). (h) The photograph of extracted tumor tissues after different treatments in each group of BALB/c mice. (i) The individual mice tumor volume change in each group of BALB/c mice. Data are shown as the mean values ± SD (n = 3). (j) The representative PCNA, TUNEL, and HE staining of tumor slices after different treatments. Scale bar: 50 μm. All the statistical significance was analyzed by ANOVA. * $p < 0.05$, ** $p < 0.01$, *** $p < 0.001$, **** $p < 0.0001$, ns, not significant.

the OPCM and the combination groups, suggesting a lower cell proliferation in the two groups. Conversely, the results of TUNEL staining showed the opposite outcomes, with the combination group showing the greatest green TUNEL FL signals and the control group showing the least FL signals, suggesting that the combination group presented the highest cell death ratio. The H&E staining results were consistent with the TUNEL and PCNA staining assays, in which excessive apoptosis and necrosis were found in the OPCM and combination groups, implying the effective antitumor effect induced by the combination of OPCM and αPD-L1. The survival time was significantly prolonged in all intervention groups compared with the control group, suggesting the long-term antitumor protection of the OMV-based nanodrugs and/or αPD-L1 (Fig. S18). Notably, there was only one mouse dead in the combination group, suggesting the effective therapeutic capacity and the long-term protective effect of the combination therapeutic paradigm. In summary, the above data suggested that the therapeutic effect of pristine OMVs was moderate, while the Cu and Mn deposited on the OMVs augmented the therapeutic efficacy of pristine OMVs for liver cancer, which was further strengthened by the combination with αPD-L1.

Since the TME of liver cancer is complex and heterogeneous, another hepatocellular carcinoma (HCC) cell line model, H22 cells, was chosen to establish BALB/c tumor-bearing mouse models to confirm the therapeutic potential of the OMV-based nanodrugs for HCC treatment. The body weight was stable in different groups, showing no unusual changes during the treatment processes (Fig. 4f). The growth of tumor relative volume, the digital photograph of dissected tumors in different groups 20 d post-treatment, the individual tumor growth curve, the extracted tumor weight, the tumor inhibition rates, and the representative digital images of H22 tumor-bearing mice, elucidated the same outcomes (Fig. 4g, 4h, 4i, S19, S20).

Apart from eliciting the high therapeutic efficacy, OPCM is also able to achieve TME-responsive T_1 weighted MR imaging due to the presence of Mn^{2+}. When Mn^{2+} ions are introduced into the body, they can interact with surrounding water molecules and accelerate the process of water molecules returning from a state of non-equilibrium to equilibrium, thus speeding up the recovery of the longitudinal magnetization vector and shortening the T_1 time. We first demonstrated the MRI performance of OPCM *in vitro*. As revealed by Fig. **S21a**, Mn concentration-dependent $1/T_1$ increase was found in all PBS systems containing 500 μg/mL OPCM. The T_1 relaxation rate was 0.7854 $mM^{-1}s^{-1}$ in pH 7.4 PBS system, 2.210 $mM^{-1}s^{-1}$ in pH 6.0 PBS system, 2.434 $mM^{-1}s^{-1}$ in pH 5.0 PBS system, and 2.636 $mM^{-1}s^{-1}$ in pH 5.0 + 10 mM GSH PBS system, among which the PBS system with pH 5.0 + 10 mM GSH displayed the strongest T1 signal and the largest T_1 relaxation rate (Fig. S21b). The above data indicated that OPCM released more Mn^{2+} in acidic environment with high GSH content, suggesting that the OPCM might release abundant Mn^{2+} in the TME. Then, we further detected its imaging capability *in vivo*. As shown in Fig. 22a and Fig. 22b, the OPCM displayed favorable T_1-weighted MRI performance. After *i.v.* injection of OPCM, the gray signal at the tumor site displayed a time-dependent increase until the 4th hour and then started to decrease until the 24th hour. The *in vivo* results suggested that OPCM efficiently accumulated in the tumor site and degraded in response to acidity and GSH in the TME, leading to Mn^{2+} release and T_1-weighted MR imaging.

To summarize, OPCM exhibited a strong antitumor effect on liver cancer models, and the effect was further amplified by αPD-L1, which might be attributed to the synergistic effect of immunogenic ferroptosis, cGAS-STING activation, and salvation of T-cell. The mechanism and the alternation of the tumor immune microenvironment will be discussed in detail in the following parts.

2.5. Exploration of immunogenic ferroptosis and cGAS-STING activation in vivo

To further clarify the underlying mechanism of OPCM-based treatments on the TME of liver cancer, the tumor tissues in each group were collected and some important proteins and markers were investigated *in vivo*. In the *in vitro* study, the OPCM was demonstrated to possess POD-like, CAT-like, and GPX-like activities. Moreover, in cellular studies, OPCM was proven to induce ferroptosis and activate the cGAS-STING signaling pathway, leading to the release of DAMPs and type 1 IFN. Hence, we conducted IF staining to verify the expression of GPX4, DHE, HIF-1α, p-STING, p-TBK1, p-IRF3, CRT, and HMGB1.

As expected, the red GPX4 signals were largely reduced in the OPCM and combination group compared with the control group, while the intervention of OMV and αPD-L1 had no significant influence on the expression of GPX4, suggesting that Cu and Mn ions in the OPCM played the key role in degrading GPX4 (Fig. 7a, 7d). Contrary to the result of GPX4, the dihydroethidium (DHE) frozen staining revealed that the OPCM and the combination groups greatly enhanced the ROS generation, while OMV had little impact on the ROS level, indicating the POD-like activity of OPCM **(**Fig. 5**a, 5e)**. Since the OPCM was capable of catalyzing H_2O_2 to generate O_2, a cellular hypoxia indicator, HIF-1α, was chosen to detect the status of tumor hypoxia. According to the IF results (Fig. 5a, 5f), the tumors in the control group displayed high expression of HIF-1α. The intervention of OMV and αPD-L1 showed negligible effects on reducing tumor hypoxia, while the bimetallic biomineralized OPCM and the combination treatments significantly reduced tumor HIF-1α signals, illustrating the intratumoral O_2 generation capability of OPCM.

Previous cellular experiments demonstrated that DNA damage induced by OPCM could activate the cGAS-STING signaling pathway, therefore we further evaluated the influence of OPCM on the cGAS-STING pathway *in vivo*. As expected, the treatment with OMV or αPD-L1 exhibited negligible effect on the expression of p-STING, p-TBK1, and p-IRF3, while the bimetallic biomineralized OPCM group and the combination group markedly enhanced the expression of the three phosphorylated proteins, corroborating that Cu and Mn deposited on the OPCM activated the cGAS-STING signaling pathway **(**Fig. 5**b, 5g, 5h, 5i)**. As reported in previous studies, CTLs and NK cells are capable of secreting IFN-γ which exacerbates ferroptosis by inhibiting system xc^- and downregulating the expression of intracellular GPX4 [23,24]. In our study, the administration of αPD-L1 was believed to activate CTLs, while OPCM was demonstrated to activate the cGAS-STING signaling pathway which further promoted DC maturation, CTL, and NK activation, resulting in abundant release of IFN-γ. As revealed by the IF staining of IFN-γ in the tumor tissues (Fig. S23), the administration of OMV slightly enhanced the expression of IFN-γ which may be attributed to the immunostimulatory effect of OMV, while the αPD-L1, OPCM, αPD-L1 + OPCM groups displayed significantly enhanced expression of IFN-γ, and the combination group showed the greatest expression, suggesting that the co-administration of αPD-L1 and OPCM activated the immunoferroptosis pathway to the greatest level. As observed in the above IF staining of GPX4, the administration of αPD-L1 down-regulated GPX4 expression. Moreover, the co-administration of both OPCM and αPD-L1 reduced the expression of GPX4 to the least as compared with other groups, confirming the immunoferroptosis pathway activated by the synergistic immunoferroptotic effect of αPD-L1 and OPCM.

To confirm the immunogenic effect of OPCM-induced ferroptosis, the expression levels of CRT and HMGB1 were measured by IF **(**Fig. 5**c, 5j, 5k)**. As shown by the IF results, the OMV and αPD-L1 slightly enhanced CRT expression and reduced the expression of intracellular HMGB1 in comparison with the control group, while the OPCM and the combination group drastically increased the expression of CRT and down-regulated intracellular HMGB1, elucidating that OPCM induced immunogenic ferroptosis.

To summarize, the OPCM exerted obvious POD-like, GPX-like, and CAT-like activities *in vivo*, resulting in GPX4/ROS-dependent immunogenic ferroptosis, tumor hypoxia alleviation, and cGAS-STING activation. Moreover, OPCM and αPD-L1-induced immune activation further amplified the intensity of ferroptosis by IFN-γ, which forms a closed-loop therapy cycle. The alteration of tumor cell signaling pathways and

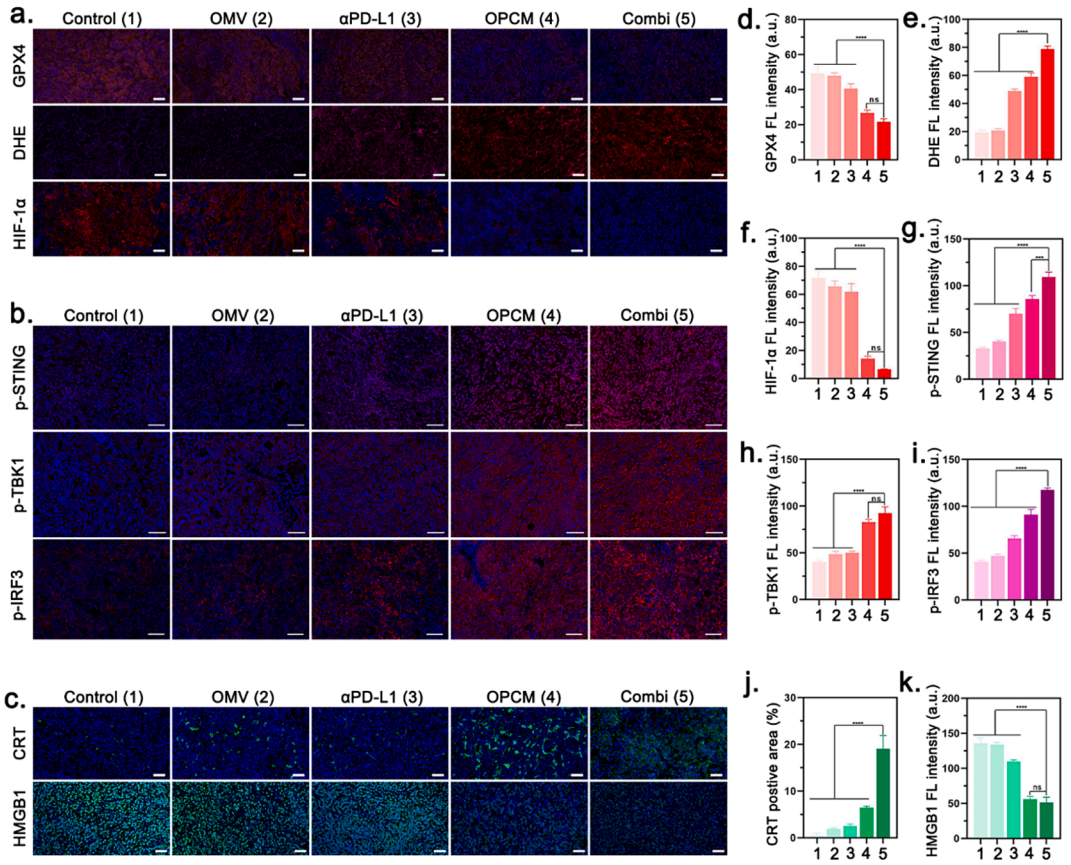

Fig. 5. The mechanism of ferroptosis induction and cGAS-STING activation *in vivo*. (a) IF staining of GPX4, DHE, HIF-1α in tumor sections after various treatments. Scale bar: 50 μm. (b) IF staining of p-STING, p-TBK1, and p-IRF3 in tumor sections after various treatments. Scale bar: 50 μm. (c) IF staining of DAMPs (CRT, and HMGB1) in tumor sections after various treatments. Scale bar: 50 μm. (d, e, f) Quantitative FL analysis of GPX4, DHE, and HIF-1α. Data are shown as the mean values ± SD (n = 3). (g, h, i) Quantitative FL analysis of p-STING, p-TBK1, and p-IRF3. Data are shown as the mean values ± SD (n = 3). (j, k) Quantitative FL analysis of CRT and HMGB1. Data are shown as the mean values ± SD (n = 3). All the statistical significance was analyzed by ANOVA. * $p < 0.05$, ** $p < 0.01$, *** $p < 0.001$, **** $p < 0.0001$, ns, not significant.

transformation of tumor metabolism may explain the mechanism of the potent antitumor effects of OPCM.

2.6. Immune cell evaluation in vivo

To delineate the immune landscape of HCC after various treatments, the infiltration level of various antitumor immune cells, including DCs, CTLs, M1 TAMs, M2 TAMs, and NK cells were analyzed by FCM. The matured DCs ($CD11c^+CD80^+CD86^+$) are crucial competent antigen professional cells (APCs) and regulate the adaptive antitumor immunity, thereby cross-priming CTLs. To investigate DC maturation, tumor tissues, tumor-draining lymph nodes (TDLNs), and spleens were harvested post-treatment for FCM analysis (**Fig. 6a, 6c**). Compared with the control group with ~12.8% intratumoral $CD80^+CD86^+$ cells, the proportion of matured DCs showed a remarkable increase in the OPCM and combination groups, particularly in the latter group with 3.9-fold increase. Similarly, the combination group displayed the highest frequency of $CD80^+CD86^+$ cells in the TDLNs (~41.3%) and spleen (~33.9%). Notably, the population of matured DCs in the OMV groups from the tumor (~28.7%), TDLNs (~24.9%), and spleen (~27.6%), was also obviously higher than that in the control group, which might be ascribed to the intrinsic immunostimulatory of OMVs on DCs as reported by previous research.[39,40] The FCM results of DC analysis in different organs clarified that OPCM was capable of promoting DC maturation which was necessary to initiate cellular immunity, and the enhancement was more pronounced in co-administration of OPCM and αPD-L1, which might be ascribed to the concerted immunostimulatory efforts of the PAMPs anchored on the OMV, abundant DAMPs outflow induced by ferroptosis, and cGAS-STING activation.

Matured DCs are professional APCs that can process tumor antigens and present them to naive T cells, thereby activating T-cell function and differentiating them into CTLs. Since the OMV-based nanodrugs were proven to promote DC maturation successfully, therefore we decided to analyze the proportion of tumoricidal CTLs within tumors, TDLNs, and spleens. As revealed by the FCM outcomes (Fig. 6**b, 6d**), compared to the control group with 6.86% $CD3^+CD8^+$ T cells in the tumors, 14.1% $CD3^+CD8^+$ T cells in the TDLNs, and 6.84% $CD3^+CD8^+$ T cells in the spleens, the treatment of OMV and αPD-L1 slightly increased the proportion of CTLs, while the combination group displayed the remarkable increase of CTLs with 3.3-fold increase in the tumor, 3.2-fold increase in the TDLNs, and 2.8-fold increase in the spleen, suggesting that the as-synthesized OPCM in combination with αPD-L1 could effectively mobilize a large number of intratumoral and systematic T cells, and prompt them differentiating into CTLs to exert tumoricidal effects.

Owing to the O_2 generation capability of Mn and Cu ions with high valence state and immunostimulatory capacity (DAMPs and inflammatory cytokines induced by OPCM, and PAMPs carried by OMVs) of OPCM, protumoral M2 TAMs can be polarized into antitumoral M1 phenotype to awaken innate antitumor immunity. To test this hypothesis, the phenotype and proportion of M1 TAMs and M2 TAMs were verified (Fig. 6**e, 6f, and 6g**). As demonstrated by FCM results, the frequency of M2 TAMs, $F4/80^+CD11b^+CD206^+$ cells, was largely decreased in the OPCM and combination groups, while the proportion of M1 TAMs, $F4/80^+CD11b^+CD80^+$ cells, was markedly promoted in these

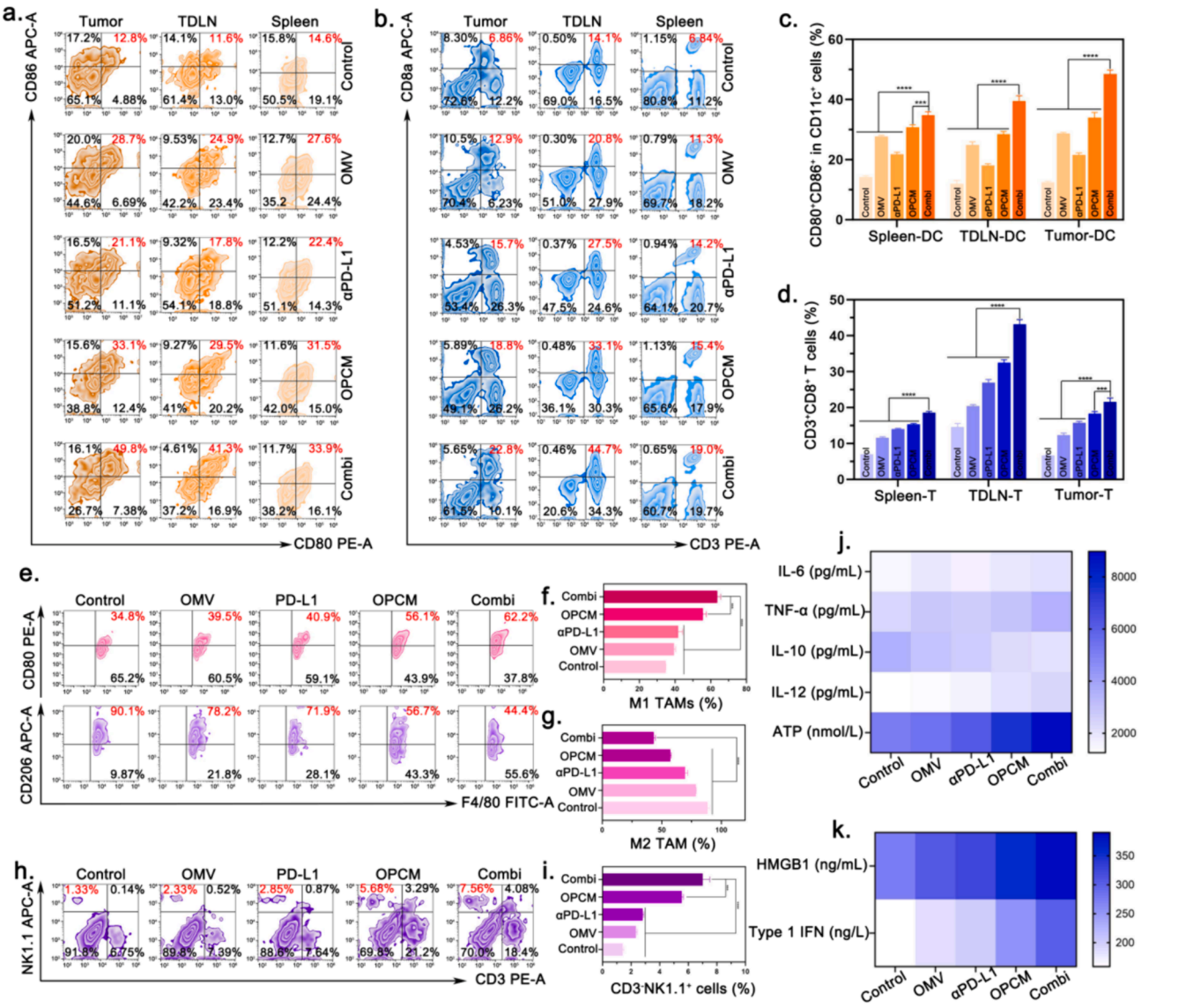

Fig. 6. The immune stimulation assay *in vivo*. (a) Representative FCM results of matured DCs ($CD11c^+CD80^+CD86^+$) within tumors, TDLNs, and spleens after different treatments. (b) Representative FCM results of CTLs ($CD3^+CD8^+$) within tumors, TDLNs, and spleens after different treatments. (c, d) Quantitative analysis of DC maturation and CTLs proportion within tumors, TDLNs, and spleens after different treatments. Data are shown as the mean values ± SD (n = 3). (e) Representative FCM results of M2 TAMs and M1 TAMs within tumors after different treatments. (f, g) Quantitative analysis of M1 TAMs and M2 TAMs within tumors after different treatments. Data are shown as the mean values ± SD (n = 3). (h, i) Representative FCM results of NK cells within tumors after different treatments and the corresponding quantitative analysis. Data are shown as the mean values ± SD (n = 3). (j, k) The secretion level of IL-6, TNF-α, IL-10, IL-12, ATP, HMGB1, and Type 1 IFN within mouse serums or tumors after various treatments. Data are shown as the mean values ± SD (n = 3). All the statistical significance was analyzed by ANOVA. * $p < 0.05$, ** $p < 0.01$, *** $p < 0.001$, **** $p < 0.0001$, ns, not significant.

two groups as compared with the control group, confirming the TAM repolarization effect of OPCM.

In addition to DCs, CTLs, and TAMs, the proportion of another innate tumoricidal immune cell, NK cell was also detected since numerous studies proved that the activation of the cGAS-STING signaling pathway could increase the population of intratumoral NK cells *via* the production of type 1 IFN. As expected, the OPCM and combination groups significantly increased the frequency of intratumoral NK cells by 4.3-fold and 5.7-fold as compared with the control group, indicating that the as-synthesized OPCM were able to mobilize NK cells to exert antitumor immunity **(**Fig. 6**h and 6i)**.

Apart from FCM analysis of the immune cell population, some crucial cytokines and immunogenic factors were detected to corroborate the alteration of the tumor immune microenvironment by ELISA. On the one hand, we collected mouse serums post-therapeutic treatment to detect the secretion level of IL-6, TNF-α, and IL-12. Fig. 6**j** showed that the serum content of pro-inflammatory cytokines, IL-6, TNF-α, and IL-12 were enhanced in all intervention groups as compared to the control group with the combination group showing the greatest enhancement, while the serum content of anti-inflammatory cytokines, IL-10 and IL-12, were downregulated in the intervention groups as compared to the control group, with the combination group displaying the lowest level of IL-10 and IL-12, indicating the effective DC maturation and TAM repolarization effects induced by OPCM. On the other hand, we extracted tumor tissues post-treatment to detect the intratumoral content of ATP, HMGB1, and type 1 IFNs (Fig. 6j, 6k). As expected, the expression levels of these three factors were markedly increased in the treatment groups with the combination group displaying the highest promotion, suggesting the induction of ICD and activation of cGAS-STING signaling pathway.

Taken together, all the above results demonstrated that the OPCM could serve as a potent immunoadjuvant to stimulate the

immunosuppressive TME by mobilizing and activating multiple immune cells from the innate and adaptive immune systems to inhibit tumor growth in combination with αPD-L1.

2.7. Long-term antitumor immune memory effect in vivo

The activation of the tumor immune microenvironment is not only conducive to killing primary tumors but also helps the body build up long-term immune memory against tumor recurrence and metastasis. Encouraged by the effective tumor suppression effect and the immunostimulatory effect of the combinational therapeutic paradigm (αPD-L1 and OPCM) achieved on the primary tumor models, tumor-re-challenged mouse and lung metastasis models were established to verify the long-term antitumor immune memory. The schematic diagrams of the establishment of both tumor models are shown in Fig. 7**a and 7j**. The body weight of re-challenged mouse models was recorded for 2 weeks since the 37th day. The tumor weight of all re-challenged mouse models remained stable during the observation process (Fig. 7b). Regarding the re-challenged tumor growth, the average tumor volume in the four intervention groups was smaller than that in the control group with 250 mm^3 (Fig. 7c). Notably, the combination group showed the slowest tumor growth with an average tumor volume of around 70 mm^3, indicating that the combination treatment possessed long-term resistance to tumor recurrence. The results of extracted tumor weight, the photograph of extracted tumors, and the representative digital photos of re-challenged mice were consistent with the outcomes of tumor volume growth, indicating that the OMV-based nanodrugs and/or αPD-L1 established long-term antitumor immune memory and thus provided long-term protection against tumor recurrence (Fig. 7d, 7e, S24).

Subsequently, the immune mechanism was further studied. TDLNs and spleens were extracted and digested to obtain a single-cell suspension, followed by FCM detection, to quantify the population of effector memory T cells (T_{em}). As revealed by the FCM results of the TDLNs, compared with only 19.1% of $CD3^+CD8^+CD44^+CD62L^-$ cells, the other four intervention groups displayed enhanced proportion of T_{em}, particularly in the OPCM and combination groups with 1.9-fold, and 2.2-fold increase, respectively **(**Fig. 7**f, 7g)**. Similarly, the FCM results of the spleens displayed the same outcome, with the combination group showing the highest proportion of T_{em} (Fig. 7h, 7i). These results indicated that the OMV-based nanodrugs combined with αPD-L1 could induce long-lasting antitumor immune memory and systemic immunity, which was beneficial for suppressing tumor recurrence via recognition of "old antigens".

To further verify that the combination paradigm of OPCM and αPD-L1 can suppress tumor metastasis, we established lung metastasis models by injecting Hepa1-6 tumor cells into the mice after various treatments through the tail vein. One week after tumor cells injection, the lung tissues of all mice were obtained, photographed, and sent for H&E staining to observe lung metastasis nodules. As revealed by Fig. 7**k** and **7l**, as compared with the four intervention groups, the H&E staining of lung sections in the control group showed a higher degree of canceration in which numerous metastasis nodules were found inhomogeneously, indicating the effective suppression of metastasis induced by OMV-based nanodrugs and/or αPD-L1 due to the activation of antitumor immune response.

In short, we demonstrated that the OMV-based nanodrugs could not only suppress the primary tumor growth by ferroptosis induction and pleiotropic immune cell mobilization but also induced long-term antitumor immune protection against tumor recurrence and metastasis *via* evoking T_{em} locally and systemically.

2.8. Evaluation of biodistribution and biosafety

Effective accumulation of OPCM in tumor sites is a prerequisite for achieving a favorable anti-tumor effect. Hence, the biodistribution of OPCM was analyzed using an *in vivo* FL imaging system. After *i.v.* DiR-labeled OPCM administration, a clear and gradually increasing FL signal was observed at the tumor site from 2h to 24h, and the FL signal reached a maximum at 24-h post-injection and reduced at 48-h post-injection as shown in Figs. S25**a and S25b**, verifying the efficient tumor accumulation of OPCM owing to the enhanced permeability and retention effect. Moreover, the mice were sacrificed at 48-h post-injection, followed by extraction of tumor tissues and major organs, including the spleen, heart, liver, lung, and kidney. *Ex vivo* FL imaging was done to capture the FL images of these tissues. The results showed that the liver displayed the highest FL signals, followed by the lung, tumor, spleen, kidney, and heart, illustrating the *in vivo* biodistribution of DiR-labeled OPCM (Fig. S25c, S25d). The high accumulation of DiR-labeled OPCM in the liver might be ascribed to the presence of Kupffer cells, sinusoidal endothelial cells, and hepatic stellate cells which can engulf abundant foreign substances.

To further detect the *in vivo* accumulation and distribution of Cu and Mn ions in tumor tissues and major organs, ICP-MS was conducted to measure the Cu and Mn content of each tissue at different time intervals **(**Fig. S25**f, S25g, S25h, S25i, S25j, S25k)**. The results showed that Cu and Mn ions preferentially accumulate in the lung, heart, and liver, which might be due to the rapid blood supply and the capture by the reticuloendothelial system, followed by metabolization and elimination of the kidney over time. Notably, the maximum contents of Mn and Cu were found in the tumor at the 4th hour, which was in accordance with the result of the MRI with the 4th hour showing the maximum imaging intensity.

To evaluate biological safety, 6–8-week-old C57BL/6J mice were treated by *i.v.* injection of OPCM at the 0th d, 1th d, 3th d, 7th d, 14th d, 21th d. At the 21st d, all mice were sacrificed and the whole blood samples, blood serums, and major organs were obtained to detect hematology parameters, liver function, and renal function markers, as well as histology observation. Fig. S25**k and S25l** displayed that all hematology parameters and biochemical indexes were within the normal range, suggesting negligible toxicity to the liver and kidney with good safety. As demonstrated by Fig. S25m the H&E staining of major organs showed no morphological abnormalities, implying no acute and chronic pathological toxicities and adverse events. The above results illustrated that OPCM was bio-compatible and posed no obvious threat to major organs, making it a feasible alternative for future clinical translation.

3. Conclusion

In conclusion, we successfully developed Cu and Mn-deposited OPCM *via* one-step biomineralization, which possessed favorable biocompatibility, TME responsiveness, and POD/CAT/GPX-like activities, leading to the initiation of tumor ferroptosis and cGAS-STING activation to modulate immune systems for liver cancer therapy. This study provided a state-of-art paradigm for treating immunosuppressive liver cancer, since the OPCM successively initiated ferroptosis and activated the cGAS-STING signaling pathway, leading to pleiotropic immune cell mobilization, including DCs, CTLs, M1 TAMs, M2 TAMs, NK cells, and T_{em}. Moreover, OPCM and αPD-L1-induced immune activation further amplified the intensity of ferroptosis by IFN-γ secretion, which formed a closed-loop therapy cycle. As a result, the systematic immunostimulation led to both primary anti-tumor immunity and long-term anti-tumor immune memory, suppressing tumor recurrence and metastasis, thus providing an innovative combination therapeutic strategy for advanced liver cancer treatment.

4. Experimental section

4.1. Chemical and materials

$MnCl_2{\cdot}4H_2O$ (13446–34-9) and $CuCl_2{\cdot}2H_2O$ (459097-5G) were obtained from Sigma Aldrich (USA). BeyoPure™ LB Broth (premixed

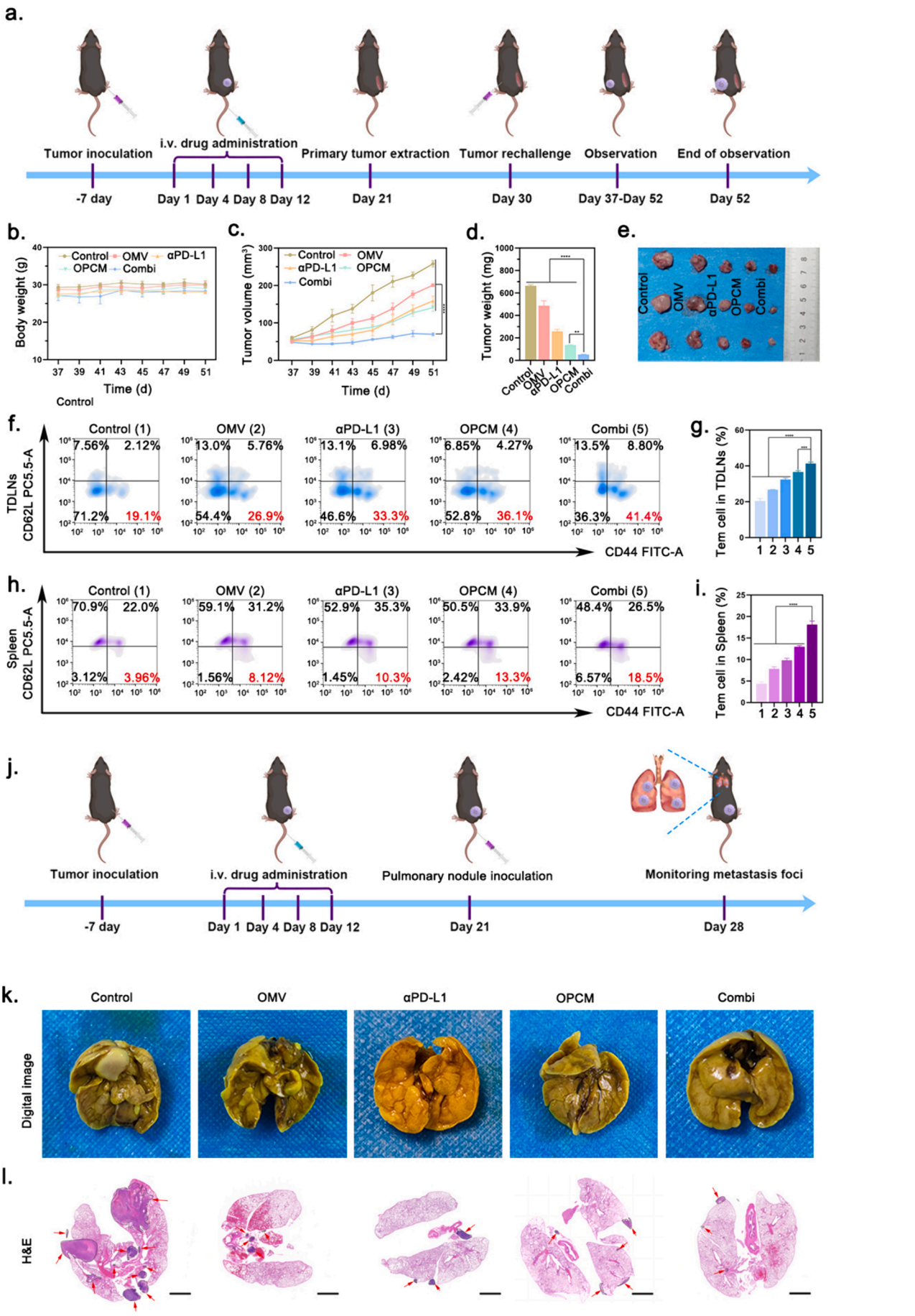

(caption on next page)

Fig. 7. Evaluation of inhibiting tumor recurrence and metastasis *in vivo*. (a) The schematic diagram of the experimental procedure for re-challenged mouse models. (b) The body weight change of re-challenged mice in different groups. Data are shown as the mean values ± SD (n = 3). (c) The contra-lateral tumor growth curve of re-challenged mice in different groups. Data are shown as the mean values ± SD (n = 3). (d) The tumor weight of extracted contra-lateral tumors in different groups. Data are shown as the mean values ± SD (n = 3). (e) The digital photograph of the extracted contra-lateral tumors in different groups. (f, g) Representative FCM results of T_{em} cells ($CD3^+CD8^+CD44^+CD62L^-$) within TDLNs and the corresponding quantitative analysis. Data are shown as the mean values ± SD (n = 3). (h, i) Representative FCM results of T_{em} cells ($CD3^+CD8^+CD44^+CD62L^-$) within spleens and the corresponding quantitative analysis. Data are shown as the mean values ± SD (n = 3). (j) The schematic diagram of the experimental procedure for lung metastasis models. (k) Representative photographs of lung tissue in mice. (i) H&E staining of lung tissue in mice. All the statistical significance was analyzed by ANOVA. * $p < 0.05$, ** $p < 0.01$, *** $p < 0.001$, **** $p < 0.0001$, ns, not significant.

powder) (ST156), protease inhibitor cocktail (P1005), and Ethylene Diamine Tetraacetic Acid (EDTA) (P1005) were bought from Beyotime Biotechnology (Jiangsu, China). HEPES-NaOH (R0088) was bought from Yuanmu Biotechnology (Shanghai, China). Hydrogen peroxide (H_2O_2, 30%) (H112517), 5,5′-dithiobis-(2-nitrobenzoic acid) ($C_{14}H_8N_2O_8S_2$, DTNB) (69-78-3), and 3,3′,5,5′-Tetramethylbenzidine ($C_{16}H_{20}N_2$, TMB) (54827-17-7) were acquired from Aladdin (Shanghai, China). The Dulbecco's modified Eagle's medium (DMEM) (PYG0073) was purchased from Boster (Wuhan, China). Streptomycin-penicillin (C0222), trypsin (C0201), DAPI staining agent (C1002), Cell Counting Kit-8 (CCK8) (C0037), DiI (C1036), DNA Damage Assay Kit (C2035S) by γ-H2AX Immunofluorescence, and JC-1 dye (C2006) were obtained from Beyotime Biotechnology (Jiangsu, China). 1,1-dioctadecyl-3,3,3,3-tetramethylindo tricarbocyanine iodide (DiR) was bought from AAT Bioquest (CA, USA) (22070). Annexin V-FITC/PI Apoptosis Kit (E-CK-A211) was bought from Elascience Biotechnology (Wuhan, China). Calcein-AM/PI Double Staing Kit (C542) and ROS assay kit (AD10) were bought from Dojindo Laboratories (Kumamoto, Japan). BODIPY-C11 (D3861) was obtained from ThermoFisher (USA). Anti-glutathione peroxidase 4 antibody (ab125066) was bought from Abcam (USA). Mouse-Reactive STING Pathway Antibody Sampler Kit (16029T) was acquired from CST (USA). Calreticulin recombinant antibody (80017-1-RR) was obtained from Proteintech (Wuhan, China). The enzyme-linked immunosorbent assays (ELISAs), including ATP (MU32950), HMGB1 (MU30043), IL-6 (MU30044), TNF-α (MU30030), Type 1 IFN (MU30047), IL-10 (MU30055), and IL-12 (MU30186) were acquired from Bioswamp (Wuhan, China). αPD-L1 antibody (BE0101) was bought from Bio X cell (USA). FITC anti-mouse CD11c antibody (117305), PE anti-mouse CD80 antibody (104707), and APC anti-mouse CD86 antibody (159215), and APC anti-mouse CD206 (141707), PE anti-mouse CD3 (100205), APC anti-mouse CD8a (162305), FITC anti-mouse F4/80 (157309), PerCP/Cyanine5.5 anti-mouse/human CD11b (101227), APC anti-mouse NK1.1 (156505), and APC anti-mouse CD8a (162305), FITC anti-mouse CD44 (156007) and PerCP/Cyanine 5.5 anti-mouse CD62L (104431) were purchased from Biolegend (San Diego, CA, USA). All the chemicals were used as purchased without further purification.

4.2. Synthesis of OMV-based nanodrugs

4.2.1. Acquirement of OMVs

OMVs was obtained according to a previously reported method. Briefly, Escherichia coli was inoculated into 250 mL LB medium and the medium was placed in a rotary shaker (180 rpm) with 37°C overnight. When OD600 of the LB medium reached 1.2, the medium was centrifuged at 5000 rpm for 10 min to collect bacteria. Afterwards, HM lysis buffer was prepared and the formula was as follows: 0.25 M sucrose, 1 mM Ethylene Diamine Tetraacetic Acid (EDTA), 20 mM HEPES-NaOH (pH 7.4), and 1x protease inhibitor cocktail. The collected bacteria were washed three times by PBS and then suspended in the HM lysis buffer. Then, the mixed solution was transferred to the ultrasonic cell disruptor in an ice bath for ultrasonic decomposition (power: 30%, time: 10 min). Subsequently, the whole solution was centrifuged at 3000 g for 5 min to eliminate the remaining bacteria and large bacterial fragments. After centrifugation, the supernatant was aspirated carefully and further underwent centrifugation at 15,000 g for 30 min to collect the sediment. The sediment was resuspended in a cold HM buffer, passing through 0.8 μm and 0.45 μm filters at least 5 times in turn to get the OMVs. To quantify OMVs, the obtained OMVs solutions were dried at 60℃ and then weighed in a precision balance.

4.2.2. Preparation of PM

First of all, whole blood was obtained from mice and then centrifuged at 200 g for 10 min at room temperature. Next, the upper platelet (PLT)-rich plasma was collected and further centrifuged at 800 g for 15 min at room temperature to collect the sediment. Cold PBS containing 1 mM EDTA and protease inhibitor was employed to suspend the PLT sediment. The mixed PLT solution was transferred thrice from room temperature to −80℃ refrigerator to obtain PLT fragments. Then, the PLT lysis was centrifuged at 4000 g for 30 min at RT to collect the sediment. Finally, the sediment was washed 3 times with PBS to obtain the pristine PM.

4.2.3. Preparation of OP, OP@Cu, OP@Mn, OCM, OPCM, and DiI or DiR-labeled OPCM

To obtain PM-coated OMVs (OP), PM and OMV were dispersed in saline with a mass ratio of 1:1. Then, the mixed solutions were put into an ultrasonic bath under 20℃ for 5 min and physically extruded 11 times by an Avanti mini extruder through a porous polycarbonate membrane (400 nm). The mixture was centrifuged (4°C, 12 000 rpm for 30 min) to obtain the OP. To obtain Cu and Mn bio-mineralized OMVs (OCM), different input concentrations of Cu and Mn (50 mM, 100 mM, 200 mM, 400 mM, 800 mM) were separately mixed with 10 mg/mL OMVs to assess the optimal input amount of $CuCl_2$ and $MnCl_2$ by ICP-MS. After confirming the best input of $CuCl_2$ (800 mM) and $MnCl_2$ (800 mM), PM was mixed with the synthesized OCM to obtain OPCM. OPCM was dispersed and stored in saline for future use. OP@Cu and OP@Mn were prepared by mixing OMV, $CuCl_2$ or $MnCl_2$, and PM similar to the preparation of OCM. DiI or DiR-labeled OPCM was prepared by mixing OPCM and DiI or DiR by physical stirring (250 rpm) for 1h at 37℃.

4.3. Characterization of various OMV-based nanodrugs, enzyme-like activities, and pharmacokinetics of OPCM in vitro

4.3.1. Characterization of various OMV-based nanodrugs

The morphology of various OMV-based nanodrugs was characterized by transmission electron microscopy (TEM) (Tecnai G2 F30 S-TWIN, USA). The elemental mapping of C, O, Cu, and Mn were also examined post TEM. The hydrodynamic diameters and zeta potentials of the OMV-based nanodrugs were analyzed by a surface zeta potential and particle size analyzer (Zetasizer Nano ZS90, Britain). Inductively coupled plasma-mass spectrometry (ICP-MS, Agilent 7700(MS), USA) was applied to quantify the content of Cu and Mn in OCM and OPCM. X-ray photoelectron spectroscopy (XPS) measurements of the valence states of Cu and Mn were obtained using the K-Alpha XPS System (Thermo Scientific K-Alpha, USA). The X-ray powder diffraction (XRD) pattern was obtained using an X-ray diffractometer (Rigaku Ultima IV, Japan).

4.3.2. Enzyme-like activities of OPCM in vitro

To test the POD-like activity of OPCM, different concentrations of OPCM (50, 200, 300, 500, and 600 μg/mL) was incubated with 10 mM H_2O_2 solution for 30 min at a 96-well plate. Then, 4 μL of TMB (80×10^{-3} M) was added into the above solutions, followed by measurement of the

wavelength absorption from 400 nm to 600 nm in a microplate reader (MultiSkan GO, Thermo scientific, USA). To track O_2 production, 0, 200, and 400 μg/mL OPCM were suspended in ultra-pure water and then sealed by paraffin. After 10 mM H_2O_2 was injected into the airtight system, a dissolved oxygen meter (JPBJ-608, Shanghai Oustor Industrial Co.) was used to measure the dissolved oxygen content for 15 min. To detect the consumption of GSH induced by OPCM, the DTNB solution was used. In brief, OPCM (500 μg/mL) were dissolved in PBS and reacted with GSH (5 mM). Afterward, the sediment was removed by centrifugation (13,000 rpm, 10 min) for various incubation durations (30 min, 1h, 2h, 4 h, 8 h, 12h, and 24h) to collect the supernatant. Finally, DTNB solution (3 mg/mL, 10 μL) was added into the supernatant in a 96-well plate, the absorbance at 412 nm was measured by a microplate reader.

4.3.3. Pharmacokinetics of OPCM in vitro

To detect the pH-responsive behavior of OPCM, OPCM was suspended in PBS solution with pH 5.0, pH 6.0, and pH 7.4. Then, the above PBS solutions containing OPCM were placed in a shaker (150 rpm, 37℃). 200 uL solutions were taken out of the three solutions at each time point (15min, 30min, 1h, 4h, 8 h, 24h, and 48h). Afterward, the 200 μL solutions were centrifuged at 15,000 rpm for 5min to obtain the supernatant for ICP-MS to detect the level of Cu and Mn.

4.4. Cellular experiments

4.4.1. Cell culture

RAW264.7 cells, Hepa1-6 cells and H22 cells were purchased from Boster (Wuhan, China). JAWSII cell was obtained from MeisenCTCC (Zhejiang, China). RAW264.7 cells, Hepa1-6 cells were cultured in DMEM containing 10% fetal bovine serum (FBS), penicillin (100 U/mL) and streptomycin (100 mg/mL) under a humidified atmosphere of 5% CO_2 at 37°C. H22 cells were cultured in RPMI-1640 medium supplemented with 10% FBS and 1% penicillin–streptomycin at 37°C with 5% CO_2. JAWSII cells were cultured in RPMI-1640 medium supplemented with 20% FBS, 1% penicillin– streptomycin, and 5 ng/mL GM-CSF at 37°C with 5% CO_2. It is worth noting that RAW264.7 cells and JAWSII are half adherent and half suspended, H22 cells are fully suspended, while Hepa1-6 cells are fully adherent. The culture medium of Hepa1-6 cells, H22 cells, and RAW264.7 cells were sub-cultured every two days, while the JAWSII cells were sub-cultured every three days. M2 TAMs were obtained by culturing RAW264.7 cells with interleukin 4 (IL- 4) (40 ng/mL) overnight.

4.4.2. Cytotoxicity of various OMV-based nanodrugs

JAWII and M2 TAMs were selected to verify the bio-compatibility of the OMV-based nanodrugs. Hepa1-6 cells were chosen to examine the anti-tumor effect of the OMV-based nanodrugs. All cell lines were seeded in 96-well plates at a density of 1×10^4 cells per well. M2 TAMs were obtained with the aforementioned method. After cell attachment, JAWSII, M2 TAMs, and Hepa1-6 cells were treated with gradient concentrations of OMV, OCM, and OPCM (50, 100, 150, 200, 250, 300 μg/mL) for 24h. After repeated washing, the cell viability was measured by the CCK-8 assay following the manufacturer's instructions.

4.4.3. The intracellular uptake of DiI-labeled OPCM

The phagocytosis of DiI-labeled OPCM was explored in Hepa1-6 cells under confocal laser scanning microscopy (CLSM) (Nikon, Tokyo, Japan) and flow cytometry (FCM) (FACS Vantage SE, Becton Dickinson, San Jose, CA, USA). For CLSM characterization, Hepa1-6 cells (1×10^5 cells per well) were separately cultured in con-focal dishes under a humidified atmosphere of 5% CO_2 at 37℃, followed by cell attachment overnight. M2 TAMs were obtained by the aforementioned method. Next, the culture medium was discarded and replaced with fresh FBS-free DMEM containing DiI-labeled OPCM, followed by co-incubation for 30 min, and 1, 2, 3, and 4h. Then, the confocal dishes were removed from the cell incubater and rinsed with PBS thrice. Afterwards, the cells were fixed with 1 mL 4% formalin for 15 min. Subsequently, the cells were washed with PBS three times and counter-stained with 100 μL DAPI staining solution for another 15 min. Finally, the cells were washed with PBS and then visualized by CLSM to take FL images to observe the cellular uptake of DiI-labeled OPCM in Hepa1-6 cells. FCM characterization was also applied for quantitative analysis. Hepa1-6 cells (2×10^5 cells per well) were cultured in 6-well plates under a humidified atmosphere of 5% CO_2 at 37℃ respectively. Then, the medium was discarded and replaced with FBS-free DMEM containing DiI-labeled OPCM, followed by co-incubation for 30 min, and 1, 2, 3, and 4h. Then, cells were collected by trypsin and suspended in 300 μL PBS solution to undergo FCM analysis.

4.4.4. Antitumor effect induced by various OMV-based nanodrugs

To further detect the antitumor effect of OMV-based nanodrugs on Hepa1-6 cells, live/dead cell staining and FCM were conducted to confirm the viability of Hepa1-6 cells after various treatments. Hepa1-6 cells (1×10^5 cells per well) were cultured in six-well plate under a humidified atmosphere of 5% CO_2 at 37℃, followed by cell attachment overnight. Afterwards, 300 μg/mL of OMV, OP, OCM, and OPCM suspending in fresh FBS-free DMEM were added into the six-well plate respectively. After co-incubation for 24h, the cells were sent for live/dead cell staining based on the manufacturer's instructions, followed by observation under an FL microscope (Nikon Ti-S, Tokyo, Japan). Simultaneously, the cells were also collected by trypsin, followed by staining of Annexin V-FITC and PI in PBS solution based on the manufacturer's instructions. Finally, FCM was performed to analyze the cell apoptotic rates of Hepa1-6 cells in various treatment groups.

4.4.5. The detection of cellular ROS generation, LPO, and MMP

Hepa1-6 cells (1×10^5 cells per well) were separately cultured in con-focal dishes under a humidified atmosphere of 5% CO_2 at 37℃, followed by cell attachment overnight. Then, the Hepa1-6 cells were divided into 5 groups and incubated with PBS, OMV, OCM, OPCM, or OPCM + Fer for 24h respectively. Afterwards, all cells were stained with DCFH-DA for detection of ROS. The cells were also stained with JC-1 dye and bodipy-C11 dye to observe variations in MMP and LPO respectively. All dishes were visualized by CLSM. In addition, cells were collected for FCM analysis of MMP. MMP was calculated as the ratio of the JC-1 aggregate/monomer.

4.4.6. Intracellular evaluation of GSH content and GPX4 expression

Hepa1-6 cells (1×10^5 cells per well) were seeded in six-well plate under a humidified atmosphere of 5% CO_2 at 37℃, followed by cell attachment overnight. Afterwards, PBS, 300 μg/mL of OMV, OCM, and OPCM suspending in fresh FBS-free DMEM were added into the six-well plate respectively. After co-incubation for 24h, cells were harvested to detect the concentration of GSH and GSSG via GSSG/GSH Quantification Kit on the one hand. On the other hand, proteins were extracted from cells to detect the expression level of GPX4 by western blot.

4.4.7. Intracellular detection of immunogenic cell death and cGAS-STING activation

Hepa1-6 cells (1×10^5 cells per well) were plated in con-focal dishes under a humidified atmosphere of 5% CO_2 at 37℃, followed by cell attachment overnight. Afterwards, PBS, 300 μg/mL of OMV, OP, OCM, and OPCM suspending in fresh FBS-free DMEM were added into the con-focal dishes respectively. After co-incubation for 24h, immunofluorescence staining of intracellular γ-H2AX and CRT was conducted to detect DNA damage and CRT exposure. Simultaneously, all cells were seeded in in six-well plate and then treated with PBS, 300 μg/mL of OMV, OCM, and OPCM suspending in fresh FBS-free DMEM for 24h. Afterwards, proteins were extracted from cells to detect the expression level of STING, p-STING, TBK1, p-TBK1, IRF3, and p-IRF3 by western blot.

4.4.8. Immune stimulation experiments induced by various OMV-based nanodrugs

A coculture transwell system (6-well plate, 0.4 μm-sized microporous membrane) was used to evaluate the immunostimulatory effect of OMV-based nanodrugs on immature DCs and M2 TAMs. JAWSII cells were seeded on the bottom of the coculture transwell system, while the Hepa1-6 cells were placed on the upper chamber. After cell attachment overnight, the old culture medium was replaced by FBS free DMEM medium containing 300 μg/mL OMV, OP, OCM, and OPCM. 24h after co-incubation, the JAWSII cells were obtained and stained with FITC CD11c antibody, PE anti-mouse CD80 antibody, and APC anti-mouse CD86 antibody following the manufacturer's instruction. Finally, the JAWSII cells underwent FCM analysis to determine the proportion of matured DCs. In addition, the supernatant of the coculture transwell system was collected and sent for ELISA to detect the secretion level of ATP, HMGB1, Type 1 IFN, IL-6, and TNF-α.

Similar to the experiment of JAWSII cells, RAW264.7 cells were seeded on the bottom of the coculture transwell system, while the Hepa1-6 cells were placed on the upper chamber. Notably, the RAW264.7 cells were first stimulated to differentiate into M2 TAMs by 40 ng/mL IL4. After cell attachment overnight, the old culture medium was replaced by FBS free DMEM medium containing 300 μg/mL OMV, OP, OCM, and OPCM. 24h after co-incubation, the JAWSII cells were obtained and stained with PE anti-mouse CD80 antibody, and APC anti-mouse CD206 antibody following the manufacturer's instruction. Finally, the RAW264.7 cells underwent FCM analysis to determine the proportion of M1 TAMs and M2 TAMs. In addition, the supernatant of the coculture transwell system was collected and sent for ELISA to detect the secretion level of ATP, HMGB1, Type 1 IFN, IL-10, and IL-12.

4.5. Animal experiment

4.5.1. Establishment of syngeneic HCC mouse models

All animal experiments were approved by the Ethics Committee of Chongqing Medical University and Institutional Animal Care. The permit number for the animal experiments is Research Ethics Review No. 223 (2023). C57BL/6J and BALB/c mice (6–8 weeks, male) were bought from the experimental animal center of Chongqing Medical University. Subcutaneous syngeneic C57BL/6J HCC mouse models were developed by injecting 5×10^6 Hepa1-6 cells suspended in 100 μL PBS into the right flanks of 6–8-week-old male C57BL/6J mice (5 mice per group). H22 tumor-bearing BALB/c mice were established by injecting 2×10^6 H22 cells suspended in 100 μL PBS into the right flanks of 6–8-week-old male BALB/c mice (3 mice per group).

4.5.2. Evaluation of antitumor effect in vivo

The schematic diagram of therapeutic and observation process for subcutaneous syngeneic HCC mouse models was shown in Fig. 6a. Subcutaneous tumors of C57BL/6J and BALB/c mice reached a measurable size 7 d post tumor cell inoculation. Then, the tumor-bearing C57BL/6J and BALB/c mice were randomly assigned to five groups, receiving saline or PBS, OMV, αPD-L1, OPCM, and the combination of αPD-L1 and OPCM on 1st, 4th, 8th, 12^{th} [38]. All mice were weighed and tumor volume was assessed once every other day. The length (L) and width (W) of tumors were measured by Vernier calipers to calculate the tumor volume (V) through the formula: $V = (L \times W^2)/2$. Photos were taken on the 1st, 5th, 10th, 15th, and 20th day. The observation for tumor treatment lasted for 20 days. Subsequently, the mice were sacrificed and the tumor tissues were extracted and weighed to calculate the tumor inhibition rate. After that, the tumor tissues extracted from C57BL/6J mice were fixed with 4% paraformaldehyde, followed by hematoxylin and eosin (H&E) staining assays and the immunofluorescent staining of terminal deoxynucleotidyl transferase dUTP nick end labeling (TUNEL) and proliferating cell nuclear antigen (PCNA). The average FL signals of TUNEL and PCNA were calculated by ImageJ. Simultaneously, survival curves of C57BL/6J mice were monitored every other day for up to 60 days after the first treatment. The mice were considered dead when the tumor volume reached 1500 mm^3.

4.5.3. Evaluation of ferroptosis and cGAS-STING activation

After 13 days, tumor tissues of each group were extracted and sent for IF staining to assess the expression of GPX4, DHE, HIF-1α, p-STING, p-TBK1, p-IRF3, CRT, and HMGB1, IFN-γ. To detect the expression of DHE, the tumor tissues of each group were frozen in −80℃ refrigerator and then sent for frozen slicing and staining of DHE working solution. Finally, the tumor sections were observed under a FL microscopy (NIKON DS-U3, Japan).

4.5.4. Evaluation of the immune cell in the TME

To study the immunostimulatory effect of the OMV-based nanodrugs, tumors, tumor-draining lymph nodes (TDLNs) and spleens were harvested from C57BL/6J mice 12 days after first treatment in different groups for immune cell analysis. Immediately after tumor tissue extraction, the TDLNs and spleens were obtained. These tissues were cut into small pieces, and digested with collagenase A (1 mg/mL), DNAase I (0.5 mg/mL) and HAase (1 mg/mL) for 30 min at 37°C. Afterward, the tissues and TDLNs were filtered to obtain single cells by 40 μm cell strainers, while spleens were filtered to obtain single cells by 70 μm cell strainers. Afterwards, the collected cells were centrifuged at 1500 rpm for 5 min and then suspended in red blood cell lysis buffer for 2 min to remove residual red blood cells. Subsequently, 1% FBS was added into the mixed cell suspension to stop digestion, followed by centrifugation at 1500 rpm for 5 min to obtain the purified cells from tumor tissues, TDLNs, and spleens. Next, the cells were stained with the corresponding fluorescence-labeled antibodies as follows: FITC anti-mouse CD11c, PE anti-mouse CD80, APC anti-mouse CD86, PE anti-mouse CD3, APC anti-mouse CD8a, FITC anti-mouse F4/80, PerCP/Cyanine5.5 anti-mouse/human CD11b, APC anti-mouse CD206, APC anti-mouse NK1.1. Finally, samples were detected by FCM. Simultaneously, tumor tissues in each group were collected for ELISA to detect the intratumoral secretion level of ATP, HMGB1, and type 1 IFNs, while serums in each group were collected for ELISA to detect the secretion level of IL-6, TNF-α, IL-10, and IL-12.

4.5.5. The establishment of tumor re-challenged models and lung metastasis models

The C57BL/6J subcutaneous models were established by the aforementioned method, followed by the same therapeutic interventions. On Day 21, primary tumors in the right flanks of mice were completely excised by surgery. After that, all mice were retained for one week. On day 30, 5×10^6 Hepa1-6 cells were rechallenged into the mice's left flanks of mice contralateral to the primary tumor site. The rechallenged tumor growth curves and weight changes were monitored once every other day from day 37 to day 51. The L and W of tumors were measured by Vernier calipers to calculate the tumor volume with the same aforementioned calculation formula. Photos were taken on the 37 d, 40 d, 43 d, 46 d, 49 d and 52 d. The observation for tumor treatment lasted for 15 days. On Day 52, all mice were sacrificed and the tumors, TDLNs, and spleens were collected. All tumor samples were weighed and photographed. TDLNs and spleens underwent the aforementioned procedure to obtain single cell suspension. Next, the cells from the tumor tissues of different treatment groups were stained with PE anti-mouse CD3 and APC anti-mouse CD8a, FITC anti-mouse CD44 and PerCP/Cyanine 5.5 anti-mouse CD62L according to the manufacturer's instructions. Finally, FCM was conducted to analyze the ratio of effector memory T (T_{em}) cells in the spleens. To establish the distant lung metastasis model, the subcutaneous models were established by the aforementioned method and treated by the same treatments. On day 21, to mimick the process of lung metastasis, the mice in each group were injected Hepa1-6 cells (1×10^6) by tail vein. On the 28 d, all mice were sacrificed and the lung were extracted, followed by staining with Bouin's solution and HE staining to observe the lung metastasis

condition.

4.5.6. FLI, MRI, and pharmacokinetics of OPCM

In vivo FLI was demonstrated using a NIRF imaging system (NightOWL II LB983, Germany) (Exc/Em = 748/780 nm). OPCM@DiR (30 mg kg^{-1}) were injected into the H22 tumor cell-bearing BALB/c mice intravenously. Then, the mice underwent FLI after certain time intervals (0, 2, 4, 8, 24, and 48h) post injection. Afterward, the mice were sacrificed, followed by extraction of the tumors and main organs for biodistribution analysis.

To detect the *in vitro* MR imaging performance of OPCM, OPCM with different concentrations (Mn: 0.13, 0.26, 0.77, 1.55, 2.58 mM) were scanned using a 3.0 T MRI scanner (MAGNETOM Prisma, Siemens Healthineers Inc., Munich, Germany). The samples were prepared in 2 mL centrifuge tube, followed by the acquisition of the T_1 weighted images (T_1WI) using the MRI scanner. The T_1WI parameters were listed as follows: fast field echo (FFE), TR = 650 ms, TE = 11 ms, and slice thickness = 1.4 mm. The T_1 relaxation rate (r_1) was calculated by the linear fitting of the inverse T_1 relaxation times as a function of Mn concentration. The T_1 relaxation rates of the acquired images were obtained through the T1 mapping data from Syngo.via software. For the MRI experiment *in vivo*, the MRI performance of the OPCM was demonstrated in H22 tumor cell-bearing BALB/c mice. A 3.0 T mouse MRI coil from Chenguang Medical Technology Company was used. The T_1WI of the tumor area was captured at different time points (0, 2, 4, 8, 12 and 24h) after the intravenous injection of the OPCM (30 mg/kg). The T_1WI parameters were set as follows: TR = 650 ms; TE = 11 ms; slice thickness = 1.5 mm; FOV = 80 mm.

To determine the *in vivo* pharmacokinetics of the OPCM, the mice were first injected with the OPCM. Then, the mice were sacrificed at each predetermined times (0, 1, 2, 4, 8, 12, 24, 48, 72h), followed extraction of tumor tissues and major organs (heart, liver, spleen, lung, kidney). All tissues were collected, weighed, dissolved with aqua regia (HCl: HNO_3 = 3:1), evaporated, and re-dissolved in 1% HNO_3. The Cu and Mn concentration was estimated by ICP-MS.

4.5.7. Bio-safety of the OPCM

The bio-compatibility of the OPCM *in vivo* was evaluated in C57 BL6/J (male, 6–8 weeks). The mice were randomly divided into six groups (control group and 1, 3, 7, 14, 21 d group after injection of OPCM, n=3). On Day 21, all mice were sacrificed. Blood samples were collected for routine blood and biochemical examinations. The major organs (heart, liver, spleen, lung, kidney) were collected for H&E analysis.

4.6. Statistical analysis

All quantitative data are shown as the mean ± SD. Statistical analysis was performed using GraphPad 10.1 (La Jolla, CA, USA). A Student's unpaired or paired *t*-test was used to analyze the significant differences between the two groups. We used the one unpaired multiple *t*-test and analysis of variance (ANOVA) for the analysis of the differences between multiple groups. Statistical tests were double-sided, and values with $P < 0.05$ were considered statistically significant.

Author contributions

Ying Luo is the first author, and Zhongsheng Xu is the parallel first author. They contributed equally to this study, including conceptualization, methodology, investigation, validation, data analysis. Specifically, Ying Luo is responsible for processing raw data and writing the manuscript, while Zhongsheng Xu is responsible for reviewing and revising the draft. Qianying Du, Lian Xu, and Yi Wang contributed partially to the methodology part. Jie Xu, Junrui Wang, Sijin Chen, Wenli Zhang, and Bo Liu contributed partially to the study administration part. Jia Liu contributed partially to the Funding part. Dajing Guo*, and Yun Liu* are the corresponding author and contributed mainly to the Funding part and paper revision.

Funding

This work was supported by the National Natural Science Foundation of China (82271970), Chongqing Medical Scientific Research Project (Joint Project of Chongqing Health Commission and Science and Technology Bureau) (Grant No. 2022ZDXM026), Senior Medical Talents Program of Chongqing for Young and Middle-aged, Chongqing Returned Overseas Students' Entrepreneurship and Innovation Support Program (cx2021006), CQMU Program for Youth Innovation in Future Medicine (W0171), and the Kuanren Doctoral supervisor Cultivation Program of the second affiliated hospital of Chongqing Medical University. This work was also supported by the General Program of Chongqing Natural Science Foundation (cstc2021jcyj-msxmX0040) and the National Science Foundation for Young Scholars (82102063).

CRediT authorship contribution statement

Ying Luo: Writing – review & editing, Writing – original draft, Project administration, Methodology, Investigation, Funding acquisition, Formal analysis, Data curation. **Zhongsheng Xu:** Writing – review & editing, Project administration, Methodology, Conceptualization. **Qianying Du:** Project administration. **Lian Xu:** Project administration. **Yi Wang:** Methodology. **Jie Xu:** Methodology. **Junrui Wang:** Methodology. **Sijin Chen:** Methodology. **Wenli Zhang:** Methodology. **Bo Liu:** Methodology. **Jia Liu:** Project administration. **Dajing Guo:** Writing – review & editing, Writing – original draft, Data curation. **Yun Liu:** Writing – review & editing, Writing – original draft, Resources, Methodology, Data curation, Conceptualization.

Declaration of competing interest

The authors declare that they have no known competing financial interests or personal relationships that could have appeared to influence the work reported in this paper.

Data availability

Data will be made available on request.

Appendix A. Supplementary data

Supplementary data to this article can be found online at https://doi.org/10.1016/j.cej.2024.155592.

References

[1] F. Xu, T. Jin, Y. Zhu, C. Dai, Immune checkpoint therapy in liver cancer, J. Exp. Clin. Cancer Res. 37 (1) (2018) 110, https://doi.org/10.1186/s13046-018-0777-4.
[2] J.M. Llovet, R.K. Kelley, A. Villanueva, A.G. Singal, E. Pikarsky, S. Roayaie, R. Lencioni, K. Koike, J. Zucman-Rossi, R.S. Finn, Hepatocellular carcinoma, Nat. Rev. Dis. Primers 7 (1) (2021) 6, https://doi.org/10.1038/s41572-020-00240-3.
[3] Y. Zheng, S. Wang, J. Cai, A. Ke, J. Fan, The progress of immune checkpoint therapy in primary liver cancer, Biochim. Biophys. Acta 1876 (2) (2021) 188638, https://doi.org/10.1016/j.bbcan.2021.188638.
[4] A. Vogel, T. Meyer, G. Sapisochin, R. Salem, A. Saborowski, Hepatocellular carcinoma, Lancet 400 (10360) (2022) 1345–1362, https://doi.org/10.1016/s0140-6736(22)01200-4.
[5] R. Donne, A. Lujambio, The liver cancer immune microenvironment: therapeutic implications for hepatocellular carcinoma, Hepatology 77 (5) (2023) 1773–1796, https://doi.org/10.1002/hep.32740.
[6] K.Y. Shen, Y. Zhu, S.Z. Xie, L.X. Qin, Immunosuppressive tumor microenvironment and immunotherapy of hepatocellular carcinoma: current status and prospectives, J. Hematol. Oncol. 17 (1) (2024) 25, https://doi.org/10.1186/s13045-024-01549-2.
[7] S.K. Wculek, F.J. Cueto, A.M. Mujal, I. Melero, M.F. Krummel, D. Sancho, Dendritic cells in cancer immunology and immunotherapy, Nat. Rev. Immunol. 20 (1) (2020) 7–24, https://doi.org/10.1038/s41577-019-0210-z.
[8] Ma, Y. Wang, Y. Zhang, S. Yang, G.R. Zhao, F.H. Xu, T cells, NK cells, and tumor-associated macrophages in cancer immunotherapy and the current state of the art

of drug delivery systems, Front. Immunol. 14 (2023) 1199173. Doi: 10.3389/fimmu.2023.1199173.
[9] B.A. Flood, E.F. Higgs, S. Li, J.J. Luke, T.F. Gajewski, STING pathway agonism as a cancer therapeutic, Immunol. Rev. 290 (1) (2019) 24–38, https://doi.org/10.1111/imr.12765.
[10] K.M. Garland, T.L. Sheehy, J.T. Wilson, Chemical and biomolecular strategies for STING pathway activation in cancer immunotherapy, Chem. Rev. 122 (6) (2022) 5977–6039, https://doi.org/10.1021/acs.chemrev.1c00750.
[11] Z.J. Long, J.D. Wang, J.Q. Xu, X.X. Lei, Q. Liu, cGAS/STING cross-talks with cell cycle and potentiates cancer immunotherapy, Mol. Ther. 30 (3) (2022) 1006–1017, https://doi.org/10.1016/j.ymthe.2022.01.044.
[12] E.N. Chin, A. Sulpizio, L.L. Lairson, Targeting STING to promote antitumor immunity, Trends Cell Biol. 33 (3) (2023) 189–203, https://doi.org/10.1016/j.tcb.2022.06.010.
[13] Y. Luo, X. He, Q. Du, L. Xu, J. Xu, J. Wang, W. Zhang, Y. Zhong, D. Guo, Y. Liu, X. Chen, Metal-based smart nanosystems in cancer immunotherapy, Exploration n/a (n/a) 20230134. Doi: 10.1002/EXP.20230134.
[14] C. Wang, Y. Guan, M. Lv, R. Zhang, Z. Guo, X. Wei, X. Du, J. Yang, T. Li, Y. Wan, X. Su, X. Huang, Z. Jiang, Manganese increases the sensitivity of the cGAS-STING pathway for double-stranded DNA and is required for the host defense against DNA viruses, Immunity 48 (4) (2018) 675–687.e7, https://doi.org/10.1016/j.immuni.2018.03.017.
[15] R.M. Hooy, G. Massaccesi, K.E. Rousseau, M.A. Chattergoon, J. Sohn, Allosteric coupling between Mn2+ and dsDNA controls the catalytic efficiency and fidelity of cGAS, Nucleic Acids Res. 48 (8) (2020) 4435–4447, https://doi.org/10.1093/nar/gkaa084.
[16] X. Sun, Y. Zhang, J. Li, K.S. Park, K. Han, X. Zhou, Y. Xu, J. Nam, J. Xu, X. Shi, L. Wei, Y.L. Lei, J.J. Moon, Amplifying STING activation by cyclic dinucleotide-manganese particles for local and systemic cancer metalloimmunotherapy, Nat. Nanotechnol. 16 (11) (2021) 1260–1270, https://doi.org/10.1038/s41565-021-00962-9.
[17] J. Yan, G. Wang, L. Xie, H. Tian, J. Li, B. Li, W. Sang, W. Li, Z. Zhang, Y. Dai, Engineering radiosensitizer-based metal-phenolic networks potentiate STING pathway activation for advanced radiotherapy, Adv. Mater. 34 (10) (2022) e2105783.
[18] Y. Zhu, Z. Yang, Z. Pan, Y. Hao, C. Wang, Z. Dong, Q. Li, Y. Han, L. Tian, L. Feng, Z. Liu, Metallo-alginate hydrogel can potentiate microwave tumor ablation for synergistic cancer treatment, Sci. Adv. 8(31) (2022) eabo5285. Doi: 10.1126/sciadv.abo5285.
[19] Q. Xiang, C. Yang, Y. Luo, F. Liu, J. Zheng, W. Liu, H. Ran, Y. Sun, J. Ren, Z. Wang, Near-infrared II nanoadjuvant-mediated chemodynamic, photodynamic, and photothermal therapy combines immunogenic cell death with PD-L1 blockade to enhance antitumor immunity, Small 18 (13) (2022) e2107809.
[20] Z. Zhao, S. Dong, Y. Liu, J. Wang, L. Ba, C. Zhang, X. Cao, C. Wu, P. Yang, Tumor microenvironment-activable manganese-boosted catalytic immunotherapy combined with PD-1 checkpoint blockade, ACS Nano 16 (12) (2022) 20400–20418, https://doi.org/10.1021/acsnano.2c06646.
[21] X. Jia, J. Wang, E. Wang, Rapid synthesis of trimetallic nanozyme for sustainable cascaded catalytic therapy via tumor microenvironment remodulation, Adv. Mater (2023) e2309261. Doi: 10.1002/adma.202309261.
[22] D. Li, E. Ha, Z. Zhou, J. Zhang, Y. Zhu, F. Ai, L. Yan, S. He, L. Li, J. Hu, "Spark" PtMnIr nanozymes for electrodynamic-boosted multienzymatic tumor immunotherapy, Adv. Mater. (2023) e2308747. Doi: 10.1002/adma.202308747.
[23] S. Guo, W. Xiong, J. Zhu, J. Feng, R. Zhou, Q. Fan, Q. Zhang, Z. Li, J. Yang, H. Zhou, P. Yi, Y. Feng, S. Yang, X. Qiu, Y. Xu, Z. Shen, A STING pathway-activatable contrast agent for MRI-guided tumor immunoferroptosis synergistic therapy, Biomaterials 302 (2023) 122300, https://doi.org/10.1016/j.biomaterials.2023.122300.
[24] J. Liu, J. Zhan, Y. Zhang, L. Huang, J. Yang, J. Feng, L. Ding, Z. Shen, X. Chen, Ultrathin clay nanoparticles-mediated mutual reinforcement of ferroptosis and cancer immunotherapy, Adv. Mater (2023) e2309562. Doi: 10.1002/adma.202309562.
[25] M. Toyofuku, N. Nomura, L. Eberl, Types and origins of bacterial membrane vesicles, Nat. Rev. Microbiol. 17 (1) (2019) 13–24, https://doi.org/10.1038/s41579-018-0112-2.
[26] M. Toyofuku, S. Schild, M. Kaparakis-Liaskos, L. Eberl, Composition and functions of bacterial membrane vesicles, Nat. Rev. Microbiol. 21 (7) (2023) 415–430, https://doi.org/10.1038/s41579-023-00875-5.
[27] Q. Chen, H. Bai, W. Wu, G. Huang, Y. Li, M. Wu, G. Tang, Y. Ping, Bioengineering bacterial vesicle-coated polymeric nanomedicine for enhanced cancer immunotherapy and metastasis prevention, Nano Lett. 20 (1) (2020) 11–21, https://doi.org/10.1021/acs.nanolett.9b02182.
[28] M.Z. Zou, Z.H. Li, X.F. Bai, C.J. Liu, X.Z. Zhang, Hybrid vesicles based on autologous tumor cell membrane and bacterial outer membrane to enhance innate immune response and personalized tumor immunotherapy, Nano Lett. 21 (20) (2021) 8609–8618, https://doi.org/10.1021/acs.nanolett.1c02482.
[29] F. Meng, L. Li, Z. Zhang, Z. Lin, J. Zhang, X. Song, T. Xue, C. Xing, X. Liang, X. Zhang, Biosynthetic neoantigen displayed on bacteria derived vesicles elicit systemic antitumour immunity, J Extracell Vesicles 11 (12) (2022) e12289.
[30] L. Chen, X. Ma, W. Liu, Q. Hu, H. Yang, Targeting pyroptosis through lipopolysaccharide-triggered noncanonical pathway for safe and efficient cancer immunotherapy, Nano Lett. 23 (18) (2023) 8725–8733, https://doi.org/10.1021/acs.nanolett.3c02728.
[31] G. Liu, N. Ma, K. Cheng, Q. Feng, X. Ma, Y. Yue, Y. Li, T. Zhang, X. Gao, J. Liang, L. Zhang, X. Wang, Z. Ren, Y.X. Fu, X. Zhao, G. Nie, Bacteria-derived nanovesicles enhance tumour vaccination by trained immunity, Nat. Nanotechnol. (2023), https://doi.org/10.1038/s41565-023-01553-6.
[32] J. Wang, W. Song, X. Wang, Z. Xie, W. Zhang, W. Jiang, S. Liu, J. Hou, Y. Zhong, J. Xu, H. Ran, D. Guo, Tumor-self-targeted "thermoferroptosis-sensitization" magnetic nanodroplets for multimodal imaging-guided tumor-specific therapy, Biomaterials 277 (2021) 121100, https://doi.org/10.1016/j.biomaterials.2021.121100.
[33] L. Kennedy, J.K. Sandhu, M.E. Harper, M. Cuperlovic-Culf, Role of glutathione in cancer: from mechanisms to therapies, Biomolecules 10 (10) (2020), https://doi.org/10.3390/biom10101429.
[34] B. Niu, K. Liao, Y. Zhou, T. Wen, G. Quan, X. Pan, C. Wu, Application of glutathione depletion in cancer therapy: enhanced ROS-based therapy, ferroptosis, and chemotherapy, Biomaterials 277 (2021) 121110, https://doi.org/10.1016/j.biomaterials.2021.121110.
[35] Y. Yang, S. Karakhanova, W. Hartwig, J.G. D'Haese, P.P. Philippov, J. Werner, A. V. Bazhin, Mitochondria and mitochondrial ROS in cancer: novel targets for anticancer therapy, J. Cell. Physiol. 231 (12) (2016) 2570–2581, https://doi.org/10.1002/jcp.25349.
[36] Z. Li, Z. Chu, J. Yang, H. Qian, J. Xu, B. Chen, T. Tian, H. Chen, Y. Xu, F. Wang, Immunogenic cell death augmented by manganese zinc sulfide nanoparticles for metastatic melanoma immunotherapy, ACS Nano 16 (9) (2022) 15471–15483, https://doi.org/10.1021/acsnano.2c08013.
[37] R. Tang, J. Xu, B. Zhang, J. Liu, C. Liang, J. Hua, Q. Meng, X. Yu, S. Shi, Ferroptosis, necroptosis, and pyroptosis in anticancer immunity, J. Hematol. Oncol. 13 (1) (2020) 110, https://doi.org/10.1186/s13045-020-00946-7.
[38] Y. Luo, J. Wang, L. Xu, Q. Du, N. Fang, H. Wu, F. Liu, L. Hu, J. Xu, J. Hou, Y. Zhong, Y. Liu, Z. Wang, H. Ran, D. Guo, A theranostic metallodrug modulates immunovascular crosstalk to combat immunosuppressive liver cancer, Acta Biomater. 154 (2022) 478–496, https://doi.org/10.1016/j.actbio.2022.10.032.
[39] O.Y. Kim, H.T. Park, N.T.H. Dinh, S.J. Choi, J. Lee, J.H. Kim, S.W. Lee, Y.S. Gho, Bacterial outer membrane vesicles suppress tumor by interferon-γ-mediated antitumor response, Nat. Commun. 8 (1) (2017) 626, https://doi.org/10.1038/s41467-017-00729-8.
[40] W. Nie, A. Jiang, X. Ou, J. Zhou, Z. Li, C. Liang, L.L. Huang, G. Wu, H.Y. Xie, Metal-polyphenol "prison" attenuated bacterial outer membrane vesicle for chemodynamics promoted in situ tumor vaccines, Biomaterials 304 (2024) 122396, https://doi.org/10.1016/j.biomaterials.2023.122396.